Journal of Environmental Management 397 (2026) 128278

Contents lists available at ScienceDirect

Journal of Environmental Management

journal homepage: www.elsevier.com/locate/jenvman

Research article

# From rock waste to reactive surfaces: Natural gabbro rocks for solar remediation of gaseous and aqueous contaminants

Gregor Žerjav [a,b,‡], Muhammad Ashraf Sabri [a,‡], Samar Al Jitan [a,§], Riccardo Tribuzio [c], Hebah Jarusheh [a], Albin Pintar [b], Khalid Al-Ali [a], Andrea Ceriani [d], Alessandro Decarlis [d,*,1], Giovanni Palmisano [a,**]

[a] *Department of Chemical and Petroleum Engineering, Research and Innovation Center on $CO_2$ and Hydrogen (RICH), Khalifa University of Science and Technology, Abu Dhabi, United Arab Emirates*
[b] *Department of Inorganic Chemistry and Technology, National Institute of Chemistry, Hajdrihova ulica 19, SI-1001, Ljubljana, Slovenia*
[c] *Dipartimento di Scienze della Terra e dell'Ambiente, Università di Pavia, Istituto Geoscienze e Georisorse, CNR, Unità di Pavia, IT-27100, Pavia, Italy*
[d] *Earth Sciences Department, Research and Innovation Center on $CO_2$ and Hydrogen (RICH), Khalifa University of Science and Technology, Abu Dhabi, United Arab Emirates*

ARTICLE INFO

*Keywords:*
Photocatalytic rocks
Gabbro
Environmental remediation
$CO_2$ fixation
$NO_2$ reduction
CO oxidation
Wastewater treatment

ABSTRACT

- This study investigates the structural, optical, and catalytic properties of mafic rock grains derived from Gabbro collected in the United Arab Emirates are to evaluate their potential as alternative catalysts for environmental applications. Nitrogen adsorption and desorption analysis revealed mesoporous and macroporous structures with low specific surface area (0.56–4.96 $m^2/g$). UV–Vis spectroscopy showed that the analyzed gabbroic rocks have band gap energies that are suitable for photocatalytic activity under illumination with visible light. The results of the photocatalytic experiments carried out under simulated sunlight showed the superior ability of the invested gabbro rock to oxidise 4-nitrophenol dissolved in water with a degradation extent of up to 65.4 %. The photodegradation of 2-propanol in air under simulated sunlight was also successful with acetone as the only formed intermediate. Thermocatalytic tests showed a significant $NO_2$ reduction activity of the investigated gabbroic rocks at temperatures above 125 °C with the highest $NO_2$ reduction rate of 17.5 %. The implementation of light radiation enabled the reduction of $NO_2$ by the studied gabbroic rock at temperatures below 120 °C. CO adsorption and its photoconversion to $CO_2$ was observed in the analyzed samples. Most of the $CO_2$ formed from CO is not released into air, as it is captured on the surface of the rocks in the form of carbonates. The high catalytic activity and CO and $CO_2$ adsorption ability can be correlated to the properties of the rocks' surface. The results underline the potential of gabbroic rocks as efficient and sustainable catalysts for pollutant degradation and $NO_2$ reduction in environmental remediation processes. These results are not only environmentally relevant for air and water quality in the various regions where gabbroic rocks occur but also pave the way for their use as commercial photocatalysts.

## 1. Introduction

Reactive nitrogen oxides ($NO_x$), carbon monoxide (CO), volatile organic compounds (VOCs) and phenolic residues remain among the most pervasive contaminants in contemporary air- and water-sheds. In 2021 the World Health Organization lowered the annual guideline values for $NO_2$ to 10 μg $m^{-3}$ and for CO to 4 mg $m^{-3}$; yet ground-level measurements show that more than three-quarters of the monitored urban population continues to inhale concentrations above these limits, with concomitant cardiopulmonary burdens and excess mortality (WHO global air quality guidelines, 2021). CO is simultaneously a regulated toxicant and a feedstock that escapes from reforming, steel and

---

* Corresponding author.
** Corresponding author.
*E-mail addresses:* alessandro.decarlis@unipg.it (A. Decarlis), giovanni.palmisano@ku.ac.ae (G. Palmisano).
[§] Current affiliation: Department of Chemistry, University of Antwerp, Belgium.
[1] Current affiliation: Dipartimento di Fisica e Geologia, Universita' degli Studi di Perugia, Perugia, Italy.
[‡] These authors contributed equally.

https://doi.org/10.1016/j.jenvman.2025.128278
Received 20 August 2025; Received in revised form 28 November 2025; Accepted 6 December 2025

petrochemical operations, while alcohol-based solvents such as 2-propanol constitute a major fraction of indoor VOC episodes. In the aqueous compartment, the electron-withdrawing nitro-group of 4-nitrophenol confers exceptional stability, so the molecule frequently survives conventional biological treatment and accumulates downstream. These multi-pollutant scenarios call for abatement processes that are simultaneous, mild in operating conditions and powered, as far as possible, by inexhaustible energy sources. Conventional methods for mitigating these pollutants, including adsorption, thermal catalytic conversion, and biological treatments, often face limitations such as high operational costs, incomplete degradation, secondary pollution, and substantial energy requirements (Badamasi, 2025; Li and Wang, 2024; Wang et al., 2025; Wang et al., 2024). Consequently, the development of sustainable, efficient, and cost-effective remediation strategies remains a priority for environmental researchers worldwide.

Photocatalytic degradation has emerged as a promising alternative due to its inherent advantages, including the utilization of abundant solar energy, ambient operational conditions, and the capability to achieve near-complete mineralization of pollutants into benign products such as $CO_2$ and water (Chen et al., 2025; Pavel et al., 2023). For instance, the photocatalytic oxidation of carbon monoxide to carbon dioxide presents an effective, environmentally benign strategy that leverages solar energy, circumventing the high temperatures and significant energy consumption associated with traditional catalytic processes (Chen et al., 2025; Pennington, 2020). Likewise, photocatalytic oxidation of 2-propanol vapors represents a green approach to air purification, effectively transforming volatile organic pollutants into harmless compounds without generating secondary contaminants (Wu and Zhong, 2025; Zhang, 2022). Furthermore, photocatalysis provides a valuable method for treating aromatic pollutants in aqueous solutions, such as 4-nitrophenol, converting them into non-toxic end products through reactive oxygen species (ROS)-mediated pathways, thus significantly improving water quality (Takhar and Singh, 2025; Liu et al., 2025; Zhang et al., 2025). The photocatalytic degradation of nitrogen dioxide ($NO_2$), particularly when integrated into photothermal catalytic approaches, represents a cutting-edge technique capable of converting $NO_2$ efficiently into environmentally benign species ($N_2$ and $O_2$). This combined effect of photocatalytic charge generation and thermal activation allows degradation to proceed under relatively mild conditions, making it an energy-efficient and sustainable alternative to conventional thermal catalysis (Xue et al., 2024; Yu, 2024).

Despite these notable advantages, photocatalysis is not without limitations. The efficiency of photocatalytic processes is significantly influenced by factors such as catalyst composition, charge carrier recombination rates, limited visible-light responsiveness, catalyst instability, and potential formation of intermediate products with unknown toxicity. Moreover, practical implementation remains constrained by challenges in catalyst recovery and reuse, necessitating research into cost-effective and stable materials with robust photocatalytic performance under solar irradiation (Chen et al., 2025; Pavel et al., 2023; Lee et al., 2023).

Prior work has demonstrated that naturally occurring rocks and minerals can participate in heterogeneous photocatalysis or serve as effective supports. For instance, basalt and granite powders have been used to discolor industrial dyes through combined adsorption–photocatalytic effects, and basalt powders have been tested as (photo-)Fenton catalysts for dye degradation (Almeida et al., 2022). Natural volcanic materials (e.g., pumice, volcanic ash) have also been used as low-cost supports for $TiO_2$ (Esparza et al., 2011), and zeolite-based composites ($TiO_2$/zeolite, ZnO/zeolite, $Fe_2O_3$/zeolite) are now a mature platform for water and air purification, including NOx removal in flow reactors (Armaković and Armaković, 2025).

Recent efforts have focused on exploring naturally abundant, stable, and cost-effective materials as potential photocatalysts. In this context, gabbro, a widespread igneous rock, emerges as an intriguing candidate for environmental remediation due to its robust mineralogical composition and physicochemical durability. Gabbro forms through the crystallization of basaltic magma trapped within the continental crust and represents a significant component of the lower oceanic crust. This rock type is frequently encountered across diverse geological settings, from mountain belts to oceanic domains. Petrologically, gabbro is the intrusive (coarse-crystalline) equivalent of basalt (fine-crystalline) and shares essentially the same bulk composition.

In the UAE, the active hard-rock quarrying industry extracts from the Semail ophiolite (Goodenough, 2010; Searle et al., 2015), where gabbro is abundant and supplies most “hard” aggregate. Therefore, gabbro tailings are the locally available, low-value byproduct to be utilized. Additionally, amphibole- and Fe/Ti-bearing phases common in gabbroic variants provide redox-active centers and visible-light absorption that (as we demonstrate) correlate with activity. For these reasons, gabbro tailings are the practical and scientifically justified choice here, even though basalt would have a similar composition.

In the United Arab Emirates (UAE), gabbro constitutes a major part of the Semail ophiolites, which form the geological backbone of the Hajar Mountains. The Semail ophiolite represents former Mesozoic oceanic crust (Tethys Ocean), tectonically emplaced against the passive Arabian continental margin, resulting in several generations of gabbroic rocks reflecting multiple magmatic events (Goodenough, 2010; Searle et al., 2015).

Characteristically, gabbro is dominated by Ca-plagioclase feldspar and pyroxenes (primarily clinopyroxene), with minor occurrences of olivine and amphibole. Plagioclase feldspars, primarily constituting albite-anorthite solid solutions, significantly contribute to the physical and chemical robustness of gabbro, making it desirable for various architectural, infrastructural, and coastal protection applications due to its hardness, durability, and aesthetic properties. Pyroxenes, characterized by their varied composition and robust crystalline structure, offer reactive surfaces potentially conducive to photocatalytic processes. Amphibole-rich varieties of gabbro, typically containing titanian pargasite, further enhance the chemical diversity of the rock and potentially amplify its photocatalytic efficacy.

This study investigates the novel application of waste-derived gabbroic rock fragments and powders from quarrying operations in the UAE, materials traditionally regarded as low-value quarry byproducts due to size constraints. By repurposing these gabbroic residues as effective photocatalysts, this research not only addresses environmental remediation challenges but also promotes economic and environmental sustainability by transforming waste into value-added resources. To the best of our knowledge, this is the first detailed study of UAE gabbro quarry tailings used directly (without functionalization) as a solar-responsive catalyst for simultaneous remediation across air ($NO_2$ reduction, CO oxidation, 2-propanol oxidation), and water (4-nitrophenol degradation) under simulated solar and visible-light irradiation.

Our work assesses unmodified UAE gabbro tailings as a standalone photocatalyst for removing both gaseous and aqueous pollutants under solar and visible light. We connect its activity to mineralogical and acidic features measured on representative quarry waste streams. Additionally, through thorough characterization and testing of various gabbro samples, this study aims to reveal the potential of gabbroic materials in advanced photocatalytic applications, supporting the broader goal of sustainable environmental remediation.

## 2. Experimental

### *2.1. Materials collection and preparation*

The material was procured from a commercial supply of inert aggregates widely utilized in construction and road-surfacing (tarmac) applications. The aggregates were extracted from multiple quarry sites located within the Hajar Mountains of the United Arab Emirates (UAE), specifically in the Emirates of Ras Al Khaimah, Fujairah, and Sharjah.

The five gabbro batches investigated here (ML, 2010; ML 105, ML

2520, ML 05, ML 32) were collected as tailings generated during the crushing and grading of construction aggregates by quarries that supply the Abu Dhabi Emirate. The intentional design choice was to evaluate whether representative waste streams, as received and without mineralogical pre-selection or functionalization, exhibit sufficient photo- and photothermal activity to support commercial waste valorization. Consequently, the codes “ML × × × × ” denote supplier batch identifiers rather than stratigraphic units; minor differences in amphibole/feldspar/pyroxene proportions, as well as Fe/Mg content (documented by XRD, XPS, and ICP), were accepted as typical of industrial feedstocks. This study therefore does not aim to identify an ‘optimal’ gabbro subtype, but to quantify the performance range and structure–function patterns across realistic quarry waste likely to be available at scale for low-cost environmental remediation.

Commercially available anatase $TiO_2$ (DT-51), supplied by CristalActive®, was utilized as a benchmark photocatalyst. The reagents 2-propanol and 4-nitrophenol were obtained from Sigma Aldrich (Germany). Gaseous reagents, namely carbon monoxide (CO), oxygen ($O_2$), Zero air, and nitrogen dioxide ($NO_2$), were sourced from Air Products Gulf Gas LLC. Elation multi element ICP (Product: 89,186.180) was obtained from VWP Chemicals (Belgium).

### 2.2. Material characterization

Five samples (ML, 2010; ML 105, ML 2520, ML 05, and ML 32) were selected from processed aggregate for detailed analysis. Rock fragments were embedded in epoxy resin and prepared as petrographic thin sections to facilitate textural and compositional characterization. Petrographic observations of mineralogical compositions were conducted using standard microscopy techniques on thin sections ranging from 30 to 50 μm in thickness. The examined rock fragments were angular to sub-angular, exhibited medium to low sphericity, and varied in size from 4 cm down to 4 mm.

Crystalline structures of the catalysts were characterized using a PANalytical Empyrean X-ray diffraction (XRD) diffractometer employing Cu Kα radiation ($\lambda = 1.54$ Å), with a scanning step size of 0.0167° across a 2θ range from 10° to 90° over a 2-h duration.

Elemental compositions were analyzed using inductively coupled plasma optical emission spectroscopy (ICP-OES) on an iCAP 7600 Duo spectrometer (Thermo Fisher Scientific, Germany), coupled with an ASX-560 autosampler from Teledyne CETAC Technologies. Prior to analysis, approximately 15 mg of each sample were digested using a CEM Mars 6 microwave digestion system (CEM Corporation, Matthews, NC, USA). Digestion involved heating the samples to 210 °C with a ramping period of 20 min from room temperature, followed by a 30-min holding period at 210 °C, in a 10 mL acid mixture of concentrated $HNO_3$, HCl, and $H_2SO_4$ (volumetric ratio of 1:3:12).

X-ray photoelectron spectroscopy (XPS) measurements were performed using an Escalab Xi + spectrometer (Thermo Fisher Scientific) equipped with a monochromatic Al Kα X-ray source (spot size of 650 μm). The analysis employed a standard lens mode with a constant analyzer energy (CAE) mode at a pass energy of 100.0 eV, an energy step size of 1.000 eV, and a total of 1361 energy steps.

Nitrogen adsorption/desorption isotherms were obtained at −196 °C utilizing a Micromeritics TriStar II 3020 analyzer. The specific surface area was calculated using the BET, and pore-size distributions were obtained by applying the Barrett–Joyner–Halenda (BJH) method. Prior to analysis, samples underwent pretreatment in a Micromeritics SmartPrep degasser under nitrogen flow (Linde, purity 6.0), initially for 60 min at 90 °C, followed by an additional 240 min at 180 °C.

The acidic properties of catalysts were investigated using a PerkinElmer Pyris 1 thermogravimetric analyzer (TGA). Samples were initially heated in air at 200 °C for 10 min and subsequently cooled to 120 °C. At this temperature, the catalyst surfaces were saturated with pyridine by exposure to a nitrogen-pyridine gas mixture for 10 min, followed by purging with pure nitrogen for an additional 90 min to remove excess pyridine. Temperature-programmed desorption (TPD) measurements were then carried out by ramping the temperature to 750 °C at a rate of 20 °C/min. Additionally, UV–Vis diffuse reflectance (UV–Vis DR) spectra were recorded using a PerkinElmer Lambda 650 spectrophotometer equipped with a Harrick Scientific Praying Mantis DRP-SAP accessory. The data were recorded in diffuse reflectance mode and absorbance trends were reported in the results.

The spectra of solid-state photoluminescence (PL) were recorded with a Horiba Fluorolog-QM 75-22-C spectrofluorometer equipped with a 75 W xenon lamp, double monochromators and a cooled R928 photomultiplier tube (PMT) detector. The measurements were performed at excitation wavelengths of 240 nm (emission range: 260–600 nm), 444 nm (465–760 nm) and 600 nm (620–870 nm) with identical settings: excitation/emission slits set to 8 nm, step size of 0.5 nm and integration time of 1 s. For measurements in the extended emission range (850–1180 nm) at 600 nm excitation, an InGaAs detector was used (slits: 8 nm, step size: 0.5 nm, integration: 0.5 s). The fluorescence lifetime was measured by time-correlated single photon counting (TCSPC) with the same instrument. Excitation was performed with a DeltaDiode 325 nm LED or a DeltaDiode 495 nm pulsed laser (spectral profiles in Fig. S1, Supplementary Material). A picosecond photon detector (Horiba, model PPD 850) replaced the PMT detector for TCSPC analysis. The instrument response function (IRF) was determined using a LUDOX SM-30 colloidal silica solution. Lifetime data were analyzed using FelixFL spectroscopy software.

Images of the catalysts’ morphology and elemental composition were obtained using a field emission scanning electron microscope (SEM, Carl Zeiss SUPRA 35 VP) equipped with an energy-dispersive X-ray detector spectrometer (EDX) Inca 400 from Oxford Instruments.

### 2.3. Photocatalytic tests

#### 2.3.1. Oxidation of 2-propanol and conversion of CO to $CO_2$

The photocatalytic oxidation of 2-propanol was evaluated under simulated solar irradiation using a LOT Quantum Design LS0606 solar simulator equipped with a 1000 W Xenon lamp and an AM1.5G filter. A gas-phase batch reactor with a volume of 340 mL containing 1 g of catalyst was initially purged with pure oxygen for 20 min. Subsequently, 2 μL of liquid 2-propanol was introduced into the reactor. The reactor was maintained in darkness for 2 h to ensure adsorption equilibrium. Throughout the experiment, temperature stability at 20 °C was achieved by circulating water through the reactor jacket. Gas-phase reaction products were periodically sampled using gas-tight syringes with capacities ranging from 0.5 to 5 mL. The collected samples were analyzed using two gas chromatographs (GCs): a Shimadzu GC-2014 equipped with both thermal conductivity (TCD) and flame ionization detectors (FID) along with a methanizer line for $CO_2$ quantification, and an Agilent 7890B GC equipped with an FID and a capillary column (Agilent, 19091N-133 HP-INNOWax, dimensions: 30 m × 250 μm × 0.25 μm) for analyzing 2-propanol and acetone.

The photocatalytic activity towards the photooxidation of carbon monoxide (CO) to carbon dioxide ($CO_2$) was assessed using the same reactor setup. The reactor was initially purged for 20 min with a gas mixture containing 100 ppm CO in zero air. After a stabilization period of 2 h in darkness, the system was illuminated using the same LS0606 solar simulator described previously. Reaction products were sampled using a 5 mL gas-tight syringe and subsequently analyzed by GC-TCD-FID (Shimadzu GC-2014).

#### 2.3.2. Liquid-phase 4-nitrophenol photodegradation reactivity test

A cylindrical beaker containing 250 mL of an aqueous solution with an initial concentration of 5 ppm 4-nitrophenol and 100 mg of catalyst was utilized as the photoreactor under continuous stirring conditions. Prior to illumination with the previously described LOT Quantum Design LS0606 solar simulator, the suspension was kept in darkness for 30 min to achieve adsorption-desorption equilibrium. A control experiment conducted in the absence of illumination was performed to determine the adsorption capacity of the gabbro samples and to verify their photocatalytic performance. Liquid aliquots were periodically collected using a syringe fitted with a 0.22 μm nylon filter and analyzed via high-performance liquid chromatography (HPLC, Thermo Scientific Dionex UltiMate 3000 with photodiode array detection). An Acclaim-120 C18 reversed-phase analytical column was employed under the following operational conditions: injection volume of 50 μL, flow rate of 0.8 mL/min, and detection wavelength set at 315 nm. The mobile phase comprised a ternary mixture of water (33 %), acetonitrile (34 %), and methanol (33 %), with all chromatographic runs conducted at ambient temperature. Following the photooxidation experiments, the extent of total organic carbon (TOC) decomposition was quantified using a Shimadzu TOC-L analyzer.

### *2.3.3. Reduction of $NO_2$*

Photocatalytic and thermocatalytic reduction experiments for the conversion of nitrogen dioxide ($NO_2$) were conducted in a temperature-controlled Harrick Praying Mantis reaction chamber, specifically designed for Raman spectroscopy studies. For optimal light absorption, the catalyst was uniformly packed to a thickness of 4 mm (approximately 120 mg). A Pfeiffer Vacuum OmniStar mass spectrometer was employed to monitor gaseous reaction products in real-time.

Initially, catalyst samples underwent a pretreatment stage by heating them in pure argon at 350 °C for 30 min. After cooling to 30 °C, a reaction gas mixture containing 5000 ppm $NO_2$ and 5 % $H_2$ in Ar, flowing at a rate of 70 mL/min, was introduced for 1 h to achieve system stabilization. Subsequently, thermocatalytic experiments were performed by heating the samples from 30 °C to 300 °C at a ramp rate of 12 °C/min, to establish the optimal temperature range for effective $NO_2$ reduction.

Photothermal experiments utilized the same pretreatment conditions, followed by controlled temperature steps from 30 °C up to 120 °C, with increments of 30 °C. At each temperature increment, catalyst stabilization was first ensured in dark conditions for 15 min, after which samples were illuminated for additional 15 min using visible light provided by a Schott KL 2500 LED light source. The energy spectrum of the employed Schott KL 2500 LED is reported in Fig. S2 of the supplementary material. The irradiance of the Schott KL 2500 LED fiber output at the sample surface was measured using a Thorlabs PM400 power meter with an S121C photodiode sensor, yielding a value of 1.04 W $cm^{-2}$. Based on the spectral distribution shown in Fig. S2 and using a spectrum-weighted average wavelength of 470 nm, corresponding to the LED emission maximum, the photon flux was calculated as $2.46 \times 10^{22}$ photons $m^{-1}$ $s^{-1}$, equivalent to $4.1 \times 10^{-2}$ mol photons $m^{-2}$ $s^{-1}$.)

## 3. Results and discussion

### *3.1. Material characterization*

The studied samples mainly contain clinopyroxene (CPX), plagioclase (PL), and minor amounts of amphibole and olivine (OL) minerals, as confirmed by the XRD results reported in Fig. 1. The composition of the samples is mostly homogeneous and represented by fragments of gabbro and olivine-gabbro.

The morphological characteristics of the investigated gabbroic rock fragments were examined by scanning electron microscopy (SEM), as shown in Fig. S3 (Supplementary Material). The SEM images reveal heterogeneous surface morphologies typical of crystalline rock fragments, characterized by angular to sub-angular particle shapes, medium-to-low sphericity, and irregular surface topography. The observed surface features include sharp edges, cleavage planes, fractures, and distinct grain boundaries, clearly indicative of brittle fracturing during sample preparation. Notably, sample ML 2520 exhibits larger, visually distinct mineral grains, whereas samples ML 05 and ML 105 display comparatively finer-grained textures and greater structural complexity.

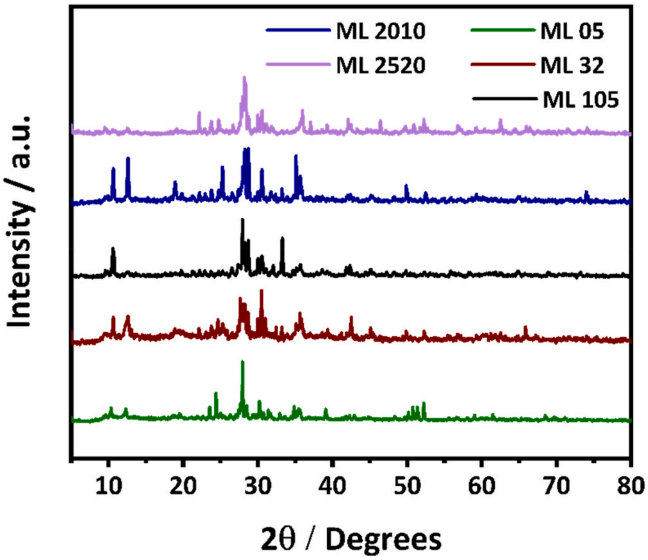

**Fig. 1.** XRD diffractograms of the investigated gabbroic samples.

The analyzed gabbroic samples predominantly comprise oxygen, silicon, aluminum, calcium, Magnesium, and iron (Table 1 – EDX results). Specifically, oxygen and silicon exhibited relatively constant atomic concentrations across all investigated samples, ranging between 46.8 and 49.1 wt% for oxygen and 19.8–23.3 wt% for silicon. Notable variability, however, was observed in the concentrations of aluminum, calcium, magnesium, and iron. Aluminum concentration varied from a minimum of 8.6 wt% in sample ML 105 to a maximum of 11.3 wt% in sample ML 05. Calcium exhibited significant variation, ranging from 6.6 wt% (ML 05) up to 12.1 wt% (ML 2520), almost double that of ML05. Magnesium content also varied notably between samples, with the highest concentration recorded in ML 2010 (7.9 wt%) and the lowest in ML 32 (4.9 wt%). Similarly, iron ranged between 2.4 wt% (ML 32) and 5.8 wt% (ML, 2010). Additionally, minor constituents detected in the samples include sodium, potassium, chromium, titanium, manganese, and sulfur, each present at atomic concentrations below 1 wt%, reflecting their subordinate role within the mineralogical composition of the gabbroic rocks.

The elemental compositions of the gabbroic samples obtained via ICP-OES analysis generally show consistency with the EDX-derived mass percentages, affirming the reliability of the compositional data despite methodological differences (Table 1). ICP results confirmed that aluminum (Al), calcium (Ca), magnesium (Mg), and iron (Fe) remain the dominant metal constituents, aligning closely with the EDX data. However, noteworthy variations are observed in the absolute elemental concentrations measured by ICP compared to EDX, likely attributable to the surface sensitivity of EDX versus the bulk sensitivity of ICP. For instance, sample ML 32 exhibited a significant disparity in Mg concentration (16.82 wt% from ICP vs. 4.9 wt% from EDX), suggesting a heterogeneous distribution of Mg-bearing phases between surface and bulk. Similar observations were evident for Al in ML 2520 (21.43 wt% ICP vs. 8.8 wt% EDX) and ML 105 (17.09 wt% ICP vs. 8.6 wt% EDX). Nevertheless, trends among samples for Fe and Ca remained comparable in both ICP and EDX analyses, confirming their relative homogeneity across samples. Minor elements such as Na, K, Cr, Ti, and Mn showed pronounced detection and quantification improvements by ICP due to its superior sensitivity, revealing higher concentrations (e.g., Mn ranging from 1.15 to 2.17 wt% ICP vs. below detection limit by EDX). Collectively, ICP-OES complements EDX by providing enhanced quantification accuracy and deeper insights into elemental distribution, which is crucial for correlating catalytic activity to compositional features in gabbroic materials. The elemental compositions of the gabbroic samples obtained via ICP-OES analysis generally show consistency with the EDX-

**Table 1**
SEM-EDX and ICP analysis of the investigated gabbro rocks.

| Element | Samples | | | | | | | | | |
|---|---|---|---|---|---|---|---|---|---|---|
| | ML 05 | | ML 32 | | ML 105 | | ML 2010 | | ML 2520 | |
| | EDX | ICP | EDX | ICP | EDX | ICP | EDX | ICP | EDX | ICP |
| O | 49.1 | n.a. | 48.2 | n.a. | 48.2 | n.a. | 47.6 | n.a. | 46.8 | n.a. |
| Si | 22.1 | n.a. | 21.3 | n.a. | 23.3 | n.a. | 19.8 | n.a. | 22.3 | n.a. |
| Al | 11.3 | 15.64 | 10.5 | 18.67 | 8.6 | 17.09 | 11.0 | 12.41 | 8.8 | 21.43 |
| Ca | 6.6 | 12.88 | 11.9 | 13.12 | 8.6 | 11.16 | 6.6 | 7.24 | 12.1 | 11.6 |
| Mg | 6.6 | 12.42 | 4.9 | 16.82 | 6.5 | 6.95 | 7.9 | 7.96 | 6.7 | 9.12 |
| Fe | 3.8 | 6.28 | 2.4 | 7.03 | 3.5 | 5.45 | 5.8 | 5.55 | 2.8 | 6.46 |
| Na | 0.4 | 1.30 | 0.8 | 1.48 | 1.2 | 0.71 | 1.2 | 0.68 | 0.5 | 1.14 |
| K | 0.04 | 1.29 | 0.02 | 1.44 | 0.01 | 0.24 | – | 1.03 | – | 0.58 |
| Cr | 0.02 | 1.78 | – | 2.02 | – | 1.57 | – | 1.93 | – | 2.17 |
| Ti | 0.02 | 1.08 | – | 0.45 | 0.08 | 0.72 | – | 0.58 | 0.03 | 0.55 |
| Mn | 0.03 | 2.06 | – | 1.94 | – | 1.18 | 0.06 | 1.15 | – | 1.3 |
| S | 0.01 | – | – | – | – | – | – | – | – | – |

derived mass percentages, affirming the reliability of the compositional data despite methodological differences. The ICP results confirmed that aluminum (Al), calcium (Ca), magnesium (Mg), and iron (Fe) remain the dominant metal constituents, aligning closely with the EDX data. However, noteworthy variations are observed in the absolute elemental concentrations measured by ICP compared to EDX, possibly attributable to the surface sensitivity of EDX versus the bulk sensitivity of ICP. For instance, sample ML 32 exhibited a significant disparity in Mg concentration (16.82 wt% from ICP vs. 4.9 wt% from EDX), suggesting heterogeneous distribution of Mg-bearing phases between surface and bulk. Similar observations were evident for Al in ML 2520 (21.43 wt% ICP vs. 8.8 wt% EDX) and ML 105 (17.09 wt% ICP vs. 8.6 wt% EDX). Nevertheless, trends among samples for Fe and Ca remained comparable in both ICP and EDX analyses, confirming their relative homogeneity across samples. Minor elements such as Na, K, Cr, Ti, and Mn were detected only by ICP due to its superior sensitivity (e.g., Mn ranging from 1.15 to 2.17 wt% ICP vs. below detection limit by EDX). Collectively, ICP-OES complements EDX by providing enhanced quantification accuracy and deeper insights into elemental distribution, which is crucial for correlating catalytic activity to compositional features in gabbroic materials.

The mineralogical compositions of the investigated gabbroic rock samples were determined using X-ray diffraction (XRD) analysis. Fig. 1 presents the XRD diffractograms of the five samples analyzed, and the results of quantitative phase identification using HighScore software are summarized in Table 2.

**Table 2**
XRD quantitative results of the investigated gabbro rocks.

| Mineral | Sample | | | | |
|---|---|---|---|---|---|
| | ML 05 | ML 32 | ML 105 | ML 2010 | ML 2520 |
| Antigorite[a] | 18 | 25 | 8 | – | – |
| Ferro-pargasite[b] | 22 | – | – | – | – |
| Albite (Ca-bearing)[c] | 35 | – | 45 | 31 | – |
| Albite[d] | – | 38 | – | – | – |
| Anorthite[e] | 25 | – | – | – | – |
| Hornblende[f] | – | 17 | 31 | 27 | 13 |
| Diopside[g] | – | 20 | 16 | – | – |
| Chlorite-serpentine[h] | – | – | – | 42 | 9 |
| Plagioclase[i] | – | – | – | – | 78 |

[a] $(Mg, Fe)_3Si_2O_5OH_4$.

[b] $NaCa_2(Fe^{2+}_4Al)(Si_6Al_2)O_{22}(OH)_2$.

[c] $(CaNa)Al_2Si_2O_8$.

[d] $(Na)Al_2Si_2O_8$.

[e] $CaNaAl_2Si_2O_8$.

[f] $(Ca,Na)_2(Mg,Fe,Al)_5(Al,Si)_8O_{22}(OH)_2$.

[g] $MgCaSi_2O_6$.

[h] $(Mg,Fe)_3(Si,Al)_4O_{10}(OH)_2\cdot(Mg,Fe)_3(OH)_6/\mathbf{Mg_3Si_2O_5(OH)_4}$.

[i] $Na(Ca)AlSi_3O_8$.

The analysis indicates that samples ML 05 and ML 105 primarily consist of anorthite-poor, Ca-bearing albite plagioclase, accounting for 35 wt% and 45 wt% of their composition, respectively. Additionally, serpentine polymorphs (antigorite) were identified in ML 05 (18 wt%) and ML 105 (8 wt%). Sample ML 05 uniquely features ferro-pargasite, constituting 22 wt% of its composition, while ML 105 contains substantial quantities of hornblende (31 wt%) and diopside (16 wt%).

Sample ML 32 predominantly comprises albite (38 wt%), accompanied by significant quantities of antigorite (25 wt%), diopside (20 wt%), and hornblende (17 wt%). The ML 2010 sample is characterized by a high content (42 wt%) of chlorite-serpentine aggregates, along with notable proportions of Ca-bearing albite (31 wt%) and hornblende (27 wt%). Lastly, ML 2520 is distinguished by its substantial plagioclase content (78 wt%), with minor inclusions of hornblende (13 wt%) and chlorite-serpentine aggregates (9 wt%). The diversity in mineral phases across these gabbroic rocks reflects variations in their geological formation processes and could influence their physical and chemical behavior in environmental remediation applications.

The mineralogical compositions obtained through XRD analysis offer valuable insights into the potential photocatalytic properties and performance of the investigated gabbroic rock samples. The dominance of plagioclase minerals such as albite and Ca-bearing albite in samples ML 105, ML 05, ML 2520, ML 32, and ML 2010 suggests structural and chemical stability during photocatalytic processes due to their inherently robust crystalline frameworks. The substantial presence of amphibole minerals, specifically hornblende in ML 105 and ML 2010 and ferro-pargasite uniquely in ML 05, is particularly significant because these minerals contain iron in various oxidation states ($Fe^{2+}$, $Fe^{3+}$), potentially enhancing visible-light absorption and redox catalytic activity through efficient charge-transfer processes. Additionally, the notable occurrence of serpentine polymorphs (antigorite) in ML 05, ML 32, and ML 105, and chlorite-serpentine aggregates in ML 2010, indicates an improved surface adsorption capacity, which can enhance pollutant-catalyst interactions and thus promote the photocatalytic degradation of organic species such as 4-nitrophenol. The presence of clinopyroxene mineral diopside in ML 32 and ML 105 further suggests enhanced catalytic activity due to active redox sites involving divalent cations ($Ca^{2+}$, $Mg^{2+}$), beneficial for reactions involving oxidation of gaseous pollutants like CO. Therefore, the diverse mineralogical characteristics reflected in XRD results rationalize the variations observed in the photocatalytic performance among the studied gabbro samples, underpinning their promising applicability for targeted environmental remediation processes.

The elemental surface compositions of the gabbroic samples obtained by XPS analysis (survey spectra – Fig. 2-a, and Table S1) indicate that oxygen and silicon are the predominant constituents across all analyzed samples, followed by aluminum, magnesium, calcium, iron, sodium, and traces of titanium, chromium, and manganese. The surface

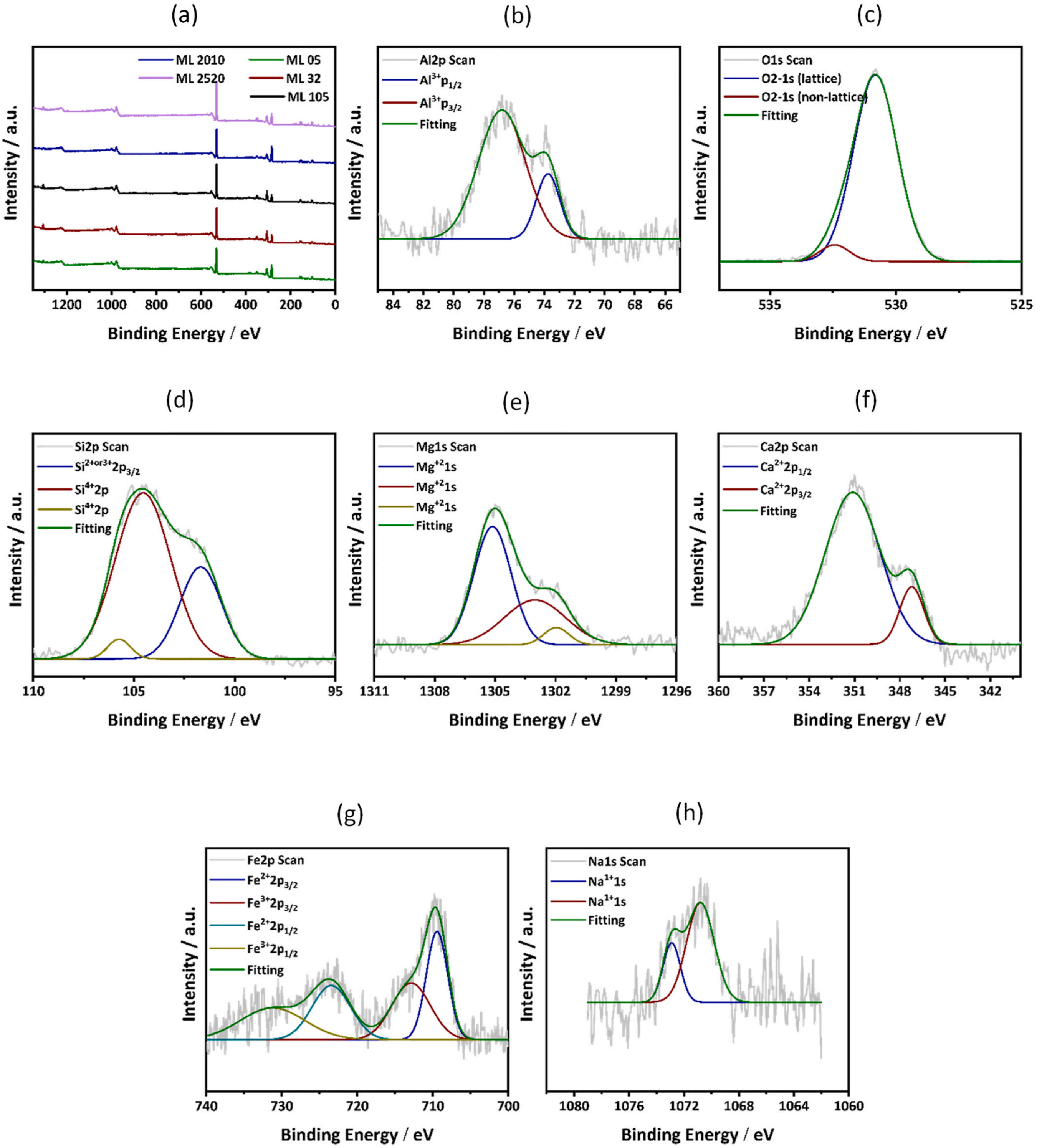

**Fig. 2.** XPS characterization of gabbroic samples: (a) Survey spectra of samples ML 05, ML 32, ML 105, ML 2010 and ML 2520. Detailed XPS scans for sample ML 05 illustrating elemental oxidation states and surface coordination environments for (b) aluminum (Al 2p), (c) oxygen (O 1s), (d) silicon (Si 2p), (e) magnesium (Mg 1s), (f) calcium (Ca 2p), (g) iron (Fe 2p), and (h) sodium (Na 1s). Fitted peaks indicate distinct oxidation states and coordination environments as discussed in the text.

elemental distribution observed by XPS generally corroborates the compositional data from EDX, highlighting oxygen as the dominant species (~64.7 at.% for ML05), with silicon (~19.2 at.%) and aluminum (~5.9 at.%) consistently abundant among all samples. Since the mineralogical compositions across the analyzed gabbroic samples exhibit substantial similarity, differing primarily in relative mineral proportions, only ML05 was selected as a representative sample for detailed XPS analysis to elucidate oxidation states and surface coordination environments relevant to catalytic behavior and surface reactivity (Fig. 2-b to 2-h, Table S2 of supplementary data). Detailed XPS results for other samples are reported in supplementary data Fig. S4–S7 and Tables S3–S6.

The aluminum present in sample ML05 (Fig. 2b) predominantly exists in the $Al^{3+}$ oxidation state, as confirmed by XPS analysis of the Al 2p region, which exhibits two distinct peaks centered around 74–75 eV (peak max = 73.75 eV) and 76–77 eV (peak max = 76.81). These peaks correspond to different aluminosilicate coordination environments: the lower binding energy peak (74–75 eV) likely represents octahedrally coordinated $Al^{3+}$ within ferro-pargasite amphibole structures, while the higher binding energy peak (76–77 eV) is attributed primarily to tetrahedrally coordinated $Al^{3+}$ present in feldspar minerals such as albite or anorthite. The Al 2p peak observed at 76.81 eV corresponds to the $Al^{3+}$ $2p_{3/2}$ state, indicative of aluminum predominantly in tetrahedral coordination ($AlO_4$) within aluminosilicate minerals. According to the International XPS Database, Al 2p binding energies vary depending on chemical environment: aluminosilicates typically occur around 74.4 eV, $Al_2O_3$ around 74.6 eV, Al–OH species like AlOOH or boehmite at ~75.7 eV, and halide-bound Al (e.g., $AlF_3$) can reach ~77.0 eV (Llc). Meanwhile, specialized XPS reference compilations (e.g., XPSfitting) note that mixed Al–O/OH/hydroxide species often result in Al $2p_{3/2}$ peaks ranging from ~75.4 to 76.4 eV, depending on hydration/coordination (Llc). The absence of peaks around 72–73 eV further confirms the lack of metallic aluminum ($Al^0$), reinforcing that aluminum is present in oxidized aluminosilicate phases within the ML05 sample.

The XPS analysis of the O 1s region for sample ML05 reveals two distinct peaks at approximately 532.43 eV and 530.81 eV (Fig. 2c). The dominant peak at 530.81 eV, which accounts for approximately 94.36 % of the peak area, is associated primarily with lattice oxygen ($O^{2-}$) present in metal oxides and silicate frameworks typical of minerals such as amphiboles, plagioclase feldspars, and pyroxenes found in gabbroic rocks. The minor peak at 532.43 eV (5.64 % of the total peak area) typically corresponds to surface-bound hydroxyl groups (–OH) or adsorbed water molecules, reflecting hydration or hydroxylation of mineral surfaces. The presence of these two peaks confirms that oxygen in ML05 predominantly exists as lattice oxygen bound within the crystal structures of silicate minerals, along with a small contribution from hydroxyl groups or adsorbed water at mineral interfaces (Lee et al., 2016). This interpretation is consistent with the mineralogical characteristics of gabbroic rocks, which contain a mixture of silicate minerals and potentially hydroxylated surface sites due to exposure to environmental moisture.

The XPS spectrum of the Si 2p region for sample ML05 reveals three distinct peaks at binding energies of approximately 105.74 eV, 104.55 eV, and 101.69 eV (Fig. 2d). The primary peak at 104.55 eV, constituting approximately 68.13 % of the total peak area, is characteristic of silicon in the $Si^{4+}$ oxidation state, typically present in tetrahedral coordination within silicate minerals such as plagioclase feldspars, amphiboles, and pyroxenes commonly found in gabbroic rocks. The peak at 105.74 eV (3.33 % area) may represent silicon in surface or hydrated silicate environments, possibly reflecting non-lattice silicon such as surface-adsorbed silicic acid species or hydrated silica (Kaur et al., 2016; Eray et al., 2020). The lowest binding energy peak at 101.69 eV (28.53 % area) indicates a less oxidized state, potentially signifying partially reduced silicon species ($Si^{2+}$, $Si^{3+}$) or sub-stoichiometric silicon oxide environments, which could be attributed to minor surface reduction processes or structural defects within the minerals (Kaur et al., 2016; Eray et al., 2020).

The XPS spectrum of the Mg 1s for sample ML05 reveals three distinct fitted peaks at binding energies of approximately 1305.13 eV, 1303.02 eV, and 1301.96 eV (Fig. 2e). The main peak at 1305.13 eV, which accounts for approximately 58.03 % of the peak area, can be assigned to $Mg^{2+}$ ions typically observed in silicate minerals such as serpentine or amphiboles. The second peak at 1303.02 eV, accounting for 36.22 % of the total peak area, also corresponds to $Mg^{2+}$ but indicates a slightly different chemical or coordination environment, likely reflecting magnesium ions in varying mineral structures or at distinct crystallographic sites within the minerals (Ye et al., 2025. The smallest peak at 1301.96 eV (5.75 % area) is also indicative of $Mg^{2+}$, potentially representing surface-related species or minor coordination variations (Chatla et al., 2022). Magnesium typically exhibits only a single oxidation state ($Mg^{2+}$) in natural minerals, and thus no lower oxidation state or elemental magnesium ($Mg^0$) peaks are observed. Furthermore, the Mg 1s core level is a singlet peak without spin-orbit splitting, unlike the Fe 2p or Ca 2p levels, simplifying the assignment to $Mg^{2+}$ across these peaks. This analysis confirms the presence of $Mg^{2+}$ ions within distinct coordination environments in the ML05 sample, consistent with its mineralogical composition comprising primarily magnesium-containing silicates such as amphiboles and serpentine.

The XPS spectrum of sample ML05 for the Ca 2p region clearly shows two peaks due to spin-orbit splitting (Fig. 2f). The peak at approximately 347.21 eV corresponds to the Ca $2p_{3/2}$ state, while the peak at 351.12 eV represents the Ca $2p_{1/2}$ state (Kumar, 2020). Both peaks confirm that calcium is exclusively present in the $Ca^{2+}$ oxidation state. The clear spin-orbit splitting and absence of lower binding energy peaks further confirm the absence of elemental calcium ($Ca^0$) and support the presence of $Ca^{2+}$ ions, most likely within calcium-bearing minerals such as plagioclase (anorthite) or amphiboles, consistent with the mineralogical composition of the analyzed rock sample.

The XPS spectrum of the Fe 2p region for sample ML05 shows multiple fitted peaks due to the characteristic spin-orbit splitting and the associated satellite structures commonly observed in iron compounds (Fig. 2g). Specifically, the Fe 2p core level splits into two principal peaks, Fe $2p_{3/2}$ and Fe $2p_{1/2}$. In ML05, the peak at approximately 709.45 eV (26.82 % peak area) can be assigned to Fe $2p_{3/2}$, predominantly indicative of $Fe^{2+}$ in iron-bearing minerals (Tolj, 2021). The peak at around 712.88 eV (25.24 % peak area) corresponds to Fe $2p_{3/2}$ typically associated with $Fe^{3+}$ species, consistent with oxidized forms of iron within silicates or oxides (Tolj, 2021). The higher binding energy peaks at 723.44 eV (24.21 % peak area) and 731.21 eV (23.73 % peak area) correspond to the Fe $2p_{1/2}$ components of $Fe^{2+}$ and $Fe^{3+}$, respectively (Tolj, 2021; Karami et al., 2021). These peaks collectively confirm the coexistence of both $Fe^{2+}$ and $Fe^{3+}$ oxidation states within the analyzed sample ML05, suggesting a mixed-valence nature of iron in the minerals, consistent with the presence of amphiboles (such as ferro-pargasite) and other iron-containing silicates identified in this rock. The clear separation and presence of satellite peaks further support this interpretation, providing a comprehensive understanding of the iron oxidation states in the ML05 sample.

The XPS analysis of the Na 1s region for sample ML05 shows two distinct fitted peaks at binding energies of approximately 1072.90 eV and 1070.81 eV (Fig. 2h). These peaks represent sodium in the $Na^+$ oxidation state (Ivanova, 2016; Kalapsazova et al., 2014), as sodium commonly occurs as $Na^+$ in geological materials and minerals. The presence of two peaks indicates two slightly different chemical or structural environments of sodium ions, potentially arising from distinct crystallographic positions within sodium-containing minerals (e.g., feldspars or amphiboles).

Tables S1–S6 summarize the XPS characterization results; Table S1 presents survey spectra data showing binding energies and atomic percentages of the surface elements across all analyzed gabbroic samples (ML 05, ML 32, ML 105, ML, 2010; and ML 2520) while Table S2 to Table S6 provides a detailed peak analysis of all five sample (ML 05, ML 32, ML 105, ML, 2010; and ML 2520), including binding energies, peak areas, oxidation states, and coordination environments of key elements.

The results of the $N_2$ adsorption/desorption analysis shown in Fig. 3 indicate that the investigated gabbro samples exhibit type IV isotherms with H3-type hysteresis loops, classifying them as mesoporous materials with slit-like interparticle pores according to IUPAC standards (Sotomayor et al., 2018), with pore sizes predominantly in the range of 2–50 nm. BJH analysis of the desorption branch (Fig. 3b–Table 3) reveals narrow pore-size distributions with mean pore diameters in the 6.9–8.1 nm range, confirming that the pore volume is predominantly associated with mesopores (2–50 nm). The distinct hysteresis loops observed suggest capillary condensation within these mesopores, a feature beneficial for photocatalytic reactions due to enhanced diffusion and interaction of reactants within the pores. Furthermore, the

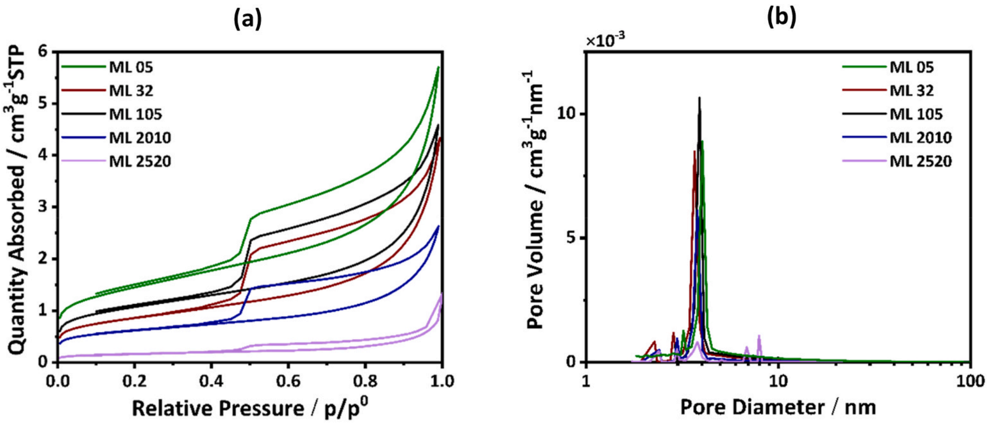

**Fig. 3.** a) $N_2$ adsorption-desorption isotherms of synthesized materials, and b) corresponding BJH pore size distributions.

**Table 3**
Textural properties (specific surface area ($S_{BET}$), pore volume ($V_{pore}$), and pore diameter ($d_{pore}$)) of the gabbro samples and $TiO_2$ benchmark. Total organic carbon (TOC) disappearance (%) measured at the end of 4-nitrophenol photooxidation runs. Concentration and surface density of acidic sites determined with the temperature programmed desorption (TPD) of pyridine on the studied solids. Band gap (BG) energies of the studied samples.

| Sample | $S_{BET}$ | $V_{pore}$ | $d_{pore}$ | TOC | Quantity of acid sites | Density of acid sites | BG |
|---|---|---|---|---|---|---|---|
| | $m^2/g$ | $cm^3/g$ | nm | % | μmol/g | μmol/$m^2$ | eV |
| ML 2010 | 2.08 | 0.004 | 7.1 | 54 | 6.9 | 3.3 | 2.66 |
| ML 105 | 3.65 | 0.007 | 7.6 | 60 | 11.0 | 3.0 | 2.77 |
| ML 2520 | 0.56 | 0.001 | 7.4 | 51 | 2.4 | 4.3 | 2.77 |
| ML 05 | 4.96 | 0.008 | 6.9 | 20 | 13.5 | 2.7 | 3.06 |
| ML 32 | 2.95 | 0.006 | 8.1 | 47 | 8.0 | 2.7 | 2.00 |
| [a]$TiO_2$ | 81.0 | 0.290 | 14.3 | 8 | / | / | 3.30 |

[a] Commercially available anatase $TiO_2$ DT-51 provided by CristalActive®.

adsorption isotherms exhibit a pronounced rise near $p/p_0 = 1$, indicative of macroporosity (>50 nm) (Bertier et al., 2016), which can facilitate efficient mass transport, thus potentially benefiting photocatalytic performance by reducing mass transfer limitations. Despite their advantageous pore features, the specific surface areas ($S_{BET}$) of the analyzed gabbroic rocks are relatively low (Table 3), ranging from 0.56 $m^2$/g (ML 2520) to 4.96 $m^2$/g (ML 05), significantly lower compared to commercial $TiO_2$ (81.0 $m^2$/g). Sample ML 05, which possesses the highest surface area among the studied solids, may offer superior photocatalytic sites due to increased surface-active sites availability. However, its relatively low photocatalytic activity in specific reactions such as 4-nitrophenol oxidation (20 % TOC removal, shown in the following) suggests that factors beyond surface area, such as band gap energy, surface acidity, and recombination dynamics of photogenerated charge carriers, significantly influence the photocatalytic performance. Samples ML 105 and ML 2010, with moderate specific surface areas (3.65 and 2.08 $m^2$/g, respectively) yet notable catalytic performance (TOC removal of 60 % and 54 %, respectively, as shown in the following), underscore the importance of balanced textural, electronic, and acidic properties in determining photocatalytic effectiveness. These results highlight the potential of mesoporous and macroporous structures in gabbroic rocks for photocatalytic applications, although further optimization of their textural and surface characteristics would likely enhance their performance relative to commercial photocatalysts.

The UV–Vis diffuse reflectance spectra (DRS) of the analyzed gabbro samples (Fig. 4a) show clear absorption features that provide information about their mineralogical and chemical composition. The spectra show significant absorption in both ultraviolet (<400 nm) and visible light (>400 nm) regions, indicating the materials' potential for photocatalytic activity in a broad spectrum of light wavelengths. The band gap energies calculated with the Kubelka-Munk function (Fig. 4b) range from 2.00 to 3.06 eV (Table 3) and reveal that the investigated gabbroic rocks are able to generate charge carriers when irradiated with visible light. A prominent absorption band appears near 260 nm, typically associated with ligand-to-metal charge transfer transitions from $O^{2-}$ to transition metal cations Singh and Singh, 2001; May and Dempsey,

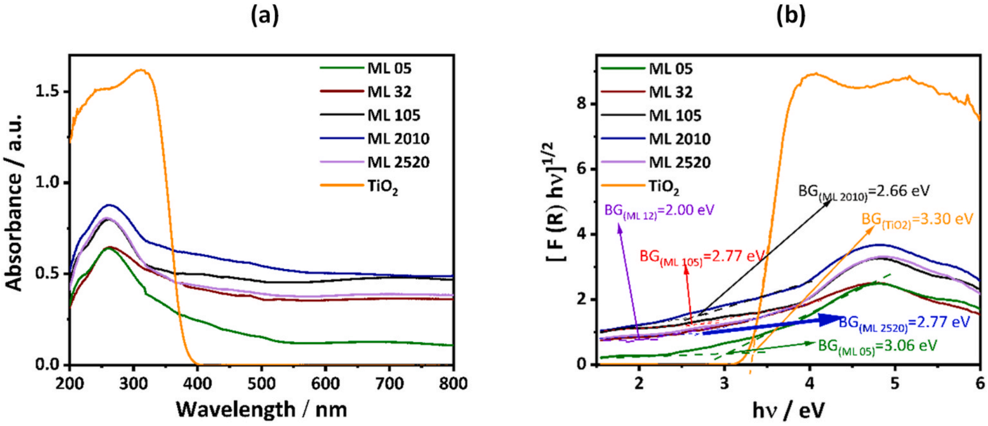

**Fig. 4.** a) UV–Vis absorbance spectra of the investigated gabbro rocks and the corresponding b) Kubelka-Munk function with the determination of the band gaps (BG) of the analyzed materials.

2024). In gabbroic samples, $Fe^{3+}$, $Ti^{4+}$, and $Cr^{3+}$ likely contribute to this feature, as these elements are known to induce such transitions when incorporated into silicate mineral lattices (Singh and Singh, 2001; May and Dempsey, 2024). Trivalent iron, especially when present in tetra- or octahedral coordination, is a well-documented cause of UV absorption (Sherman, 1985; Malik et al., 2020). Similarly, even traces of titanium and chromium can significantly affect UV–Vis spectra through strong charge transfer interactions. In the visible region (400–800 nm), the spectra exhibit broad absorption features that are characteristic of electronic d–d transitions in the d- orbitals of transition metal ions, especially $Fe^{2+}$ and $Fe^{3+}$. $Fe^{2+}$ typically contributes to absorptions ranging from the near infrared to the red region of the visible spectrum, while $Fe^{3+}$ produces broad bands in the blue to green region (400–600 nm) depending on its crystal field environment (Saito, 2025; Lin et al., 2013). In addition, the intermittent charge transfer between $Fe^{2+}$ and $Fe^{3+}$ ions likely contributes to the continuous absorption observed throughout the visible spectrum. This broad absorption profile is consistent with the characteristic dark, greenish-grey coloration of the investigated gabbroic rocks. Some samples also show localized absorption features around 700 nm. These bands are less intense, but still significant, and may originate from d–d transitions of $Mn^{3+}$, which is known to absorb in the red to near-infrared region (Czaja et al., 2018). $Fe^{3+}$ ions in distorted octahedral sites may also contribute to this feature. The presence of $Cr^{3+}$, even in trace amounts, can further explain the absorption around 680–700 nm, depending on the structure of the host mineral (Taran et al., 1994). Moreover, defined absorption features near 700 nm may indicate the presence of Fe-rich secondary minerals such as chlorite or serpentine, especially under geochemical conditions that favor their formation (Kamps et al., 2018). These minerals often exhibit diagnostic spectral signatures in this range when they are enriched in iron relative to magnesium.

Solid-state PL measurements in which gabbro samples were excited at 240 nm were recorded and the PL emission was acquired in the range between 260 and 600 nm (Fig. 5a). A minor emission peak was obtained at 300 nm, which is probably due to the intrinsic luminescence of the silicate framework, especially related to defect states in the silica-rich mineral matrix. In silicate minerals, such emissions in the UV range can originate from non-bridging oxygen hole centers, oxygen vacancies or self-trapped excitons (Song et al., 2000; Sułowska et al). These are intrinsic lattice defects that often form during geological processes, especially under high pressure and temperature conditions to which gabbro is exposed during its formation in the lower crust. The intense emission at 400 nm is most likely due to defect-induced luminescence or impurity-induced transitions, especially in $Fe^{3+}$, $Ti^{4+}$ or possibly $Cr^{3+}$. When excited with high-energy UV light (e.g. 240 nm), charge transfer transitions can occur, most commonly from $O^{2-}$ to $Fe^{3+}$ and the recombination of these excited states can lead to photon emission in the violet to blue range (Devaraja, 2015; Page et al., 2010; Kumar et al., 2003). $Ti^{4+}$, when present in a distorted octahedral environment, can also contribute to blue luminescence through charge transfer mechanisms. The strong intensity of the 400 nm peak indicates that these types of recombination centers are relatively common or highly efficient in the studied gabbroic rocks (Somakumar, 2023).

When the gabbroic rock samples were excited at 444 nm and the emission measured in the range from 465 to 760 nm (Fig. 5b), a clear emission peak was observed at 490 nm, followed by a gradual decrease in intensity with a tail extending to longer wavelengths. The peak at 490 nm is in the blue-green region of the visible spectrum and is characteristic of $Mn^{2+}$ ions substituted in silicate mineral lattices. In particular, $Mn^{2+}$ in tetrahedral or distorted octahedral coordination often emits at wavelengths between 480 and 520 nm due to the $^4T_1 \rightarrow {}^6A_1$ transition, which is spin-forbidden but can become partially allowed depending on

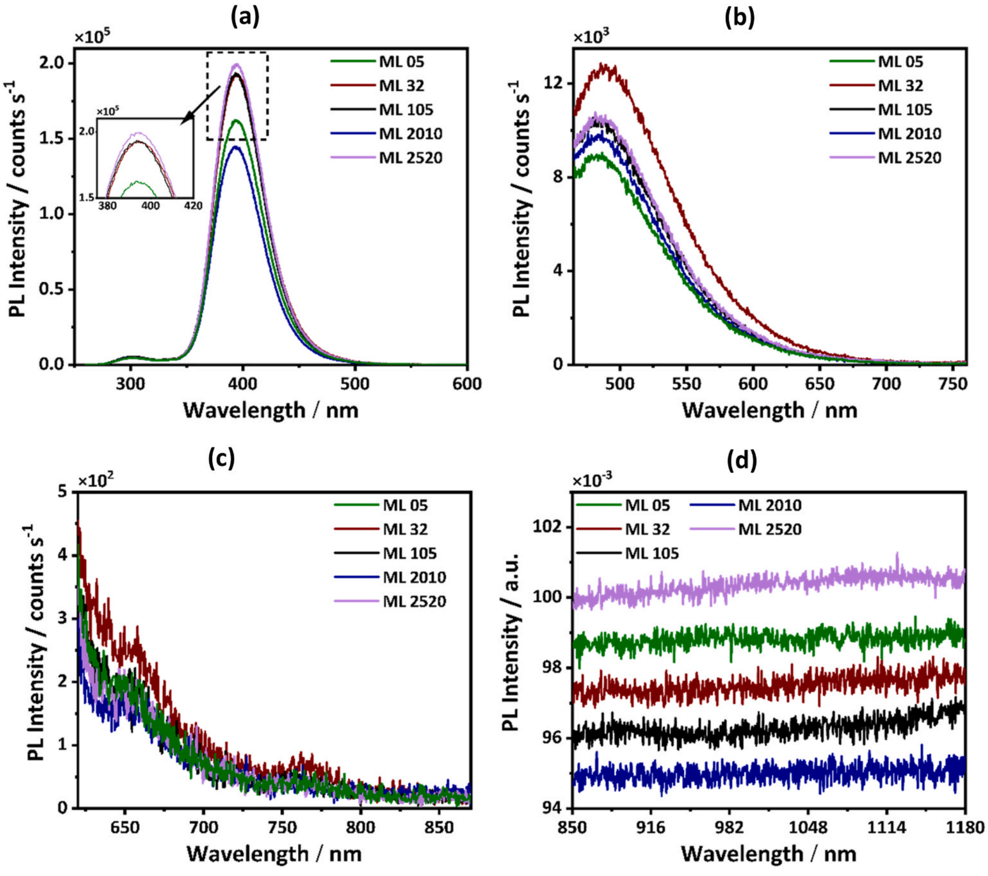

**Fig. 5.** Results of solid-state photoluminescence (PL) measurements of the investigated gabbroic rocks, performed with Xe light excitation at a) 240 nm, b) 444 nm and c) 600 nm using a PMT detector. The measurements shown in Figure d were carried out under 600 nm excitation with an InGaAs detector.

the symmetry of the local environment (Artem'ev et al., 2019; Abdel-Hameed et al., 2019). Such emissions are commonly seen in feldspar minerals found in many gabbroic rocks and reflect the presence of trace amounts of Mn incorporated during mineral crystallization (Gaft et al., 2005). The broad tail that follows the peak and extends to about 750 nm indicates the presence of multiple overlapping emission processes or defect-related recombination pathways. This type of gradual decrease in intensity is typical of phonon-coupled luminescence, where the excited electrons interact with lattice vibrations before recombining, as well as transitions from structural defects or $Fe^{3+}$ centers that emit weaker and over broader energy ranges (Somakumar, 2023).

Solid-state PL measurements were also carried out at an excitation wavelength of 600 nm. The results in Fig. 5c show a weak emission signal that starts at 620 nm and gradually decreases in intensity until about 750 nm, after which no further emission is observed. This spectral behavior indicates that the excitation energy at 600 nm (which corresponds to about 2.07 eV) is probably too low to efficiently excite the main luminescence centers in the sample. The observed weak emission, which decays at 750 nm, indicates the presence of low efficiency recombination processes or residual emission from defect-related states, but no strong or well-defined emission centers are active under this excitation (Guesmi, 2023). There are several possible explanations for this behavior. One of these is the inefficient excitation of transition metal ions. At 600 nm, the excitation energy is not sufficient to trigger charge transfer transitions or high-energy d–d transitions in $Fe^{3+}$, $Ti^{4+}$ or $Cr^{3+}$, which are responsible for the stronger emissions observed at shorter wavelengths (e.g. 240 or 444 nm) (Gao, 2025; Ichikawa et al., 2022. Another possible explanation could be the lack of suitable luminescence centers in this spectral range. Common NIR-active rare earths (e.g. $Nd^{3+}$, $Er^{3+}$, $Yb^{3+}$), emitting in this range, are either not present in our analyzed samples or below the detection limit (Rabouw et al., 2018). The results of the XRD and SEM-EDX elemental analysis (see text below) support this assumption, as such lanthanides could not be detected. In addition, Fe-related quenching could also occur. Iron, especially $Fe^{2+}$ and $Fe^{3+}$, can act as a luminescence quencher in silicate matrices and suppress the emission from nearby centers. This effect is stronger at lower excitation energies, where inefficient excited states can be further deactivated in a non-radiative manner (Wei, 2019). Finally, measurements with 600 nm excitation using an InGaAs detector in the near infrared range between 850 and 1180 nm showed no emission from the samples (Fig. 5d). The absence of luminescence in the near infrared suggests that the examined gabbroic rock does not contain NIR-active luminescent centers, such as rare earth ions, which are normally responsible for emissions in this spectral range. In addition, the relatively high concentrations of iron in the samples probably promote non-radiative quenching mechanisms that suppress possible luminescence at longer wavelengths. The photoluminescence behavior of the studied gabbroic rock samples reflects the presence of defect centers and traces of transition metal ions (especially $Mn^{2+}$, $Fe^{3+}$, $Ti^{4+}$) embedded in the silicate mineral matrix. These centers are effectively excited by high-energy UV and blue light, resulting in emissions in the 300–500 nm range, with weaker and broad emissions extending into the red region. In contrast, low energy excitation (600 nm) does not produce significant luminescence and no NIR emission is observed, confirming the absence of rare earths or NIR active defect centers.

Time-correlated single photon counting (TCSPC) analysis was performed on the examined gabbro rock samples to investigate the dynamics of charge carrier recombination after excitation at different wavelengths. The average photoluminescence decay time of charge carriers ($\tau_{aver}$) in the examined solids were extracted from the decay curves (Figs. S8 and S9) obtained upon excitation of the investigated materials at 325 nm (DeltaDiode LED light source) and 495 nm (DeltaDiode laser light source) by using a multi-exponential fitting:

$$\tau_{aver} = \frac{\sum A_i \tau_i^2}{\sum A_i \tau_i} \qquad (1)$$

where $A_i$ are the amplitudes/weighting (pre-exponential) factors and $\tau_i$ corresponding lifetimes (Table S7, supplementary data). Interestingly, the rank order of the $\tau_{aver}$ of the investigated rocks observed at these two excitation wavelengths (Fig. 6 and Table S7, supplementary data) were of opposite nature, indicating fundamentally different recombination mechanisms or activation of the luminescent centers depending on the excitation energy (D'Amico et al., 2009). The excitation at 325 nm corresponds to a relatively high photon energy in the near UV range, which is sufficient to excite charge carriers across wide band gaps or to transport electrons from the valence band to higher energy defect states or transition metal centers. This higher energy excitation is likely related to intrinsic defects in the silicate lattice, such as oxygen vacancies, non-bridging oxygen hole centers or self-trapped excitons, as well as charge transfer transitions involving $Fe^{3+}$ or $Ti^{4+}$ ions (D'Amico et al., 2009). The recombination lifetimes under this excitation therefore reflect the dynamics of these high-energy electronic states and their associated defect complexes. On the other hand, excitation at 495 nm corresponds to a lower photon energy in the visible range, which can selectively excite different luminescence centers, such as $Mn^{2+}$ ions or other transition metal impurities embedded in the silicate matrix (Gao, 2025). These centers often have narrower energy levels and exhibit different electron-phonon coupling strengths, which can lead to different recombination rates compared to the higher energy states reached at 325 nm. The observed opposite trends in average lifetimes suggest that the processes dominating luminescence at these two excitation energies are different and may even compete with each other. For example, a longer lifetime at 325 nm excitation could indicate fewer non-radiative pathways and more stable excited states associated with intrinsic defects or charge transfer centers, while the shorter lifetime at 495 nm could imply more efficient non-radiative relaxation or stronger quenching of $Mn^{2+}$ or other impurity-related emissions. Conversely, a shorter lifetime at 325 nm and a longer lifetime at 495 nm could indicate fast recombination of high-energy carriers and more stable luminescence of impurity centers at lower excitation energy. In addition, the difference in lifetimes may be influenced by the local crystal field environment, defect concentration and the presence of quenching ions such as $Fe^{2+}$ and $Fe^{3+}$, which are known to facilitate non-radiative decay channels. These factors influence the balance between radiative and non-radiative recombination and thus characterize the overall luminescence decay dynamics. The TCSPC results illustrate the complex photophysical behavior of gabbroic rocks in which multiple luminescence centers with different recombination kinetics coexist.

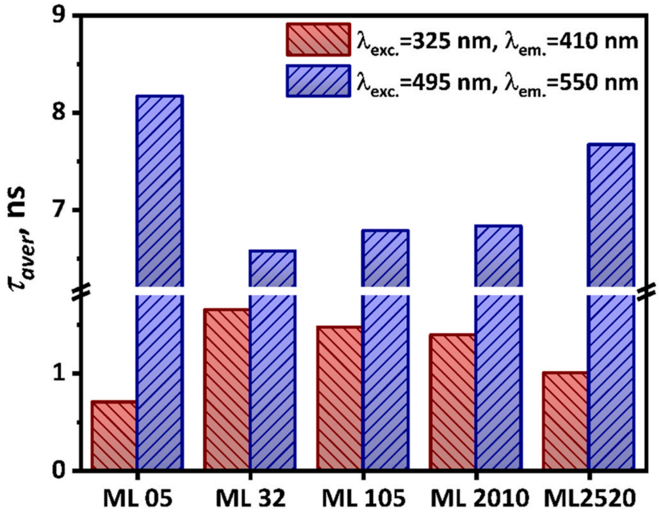

**Fig. 6.** The diagram illustrates the increase in the average lifetime ($\tau_{aver}$) of the gabbroic rocks analyzed, as determined from the various light excitations shown in Table S7 and Figs. S8 and S9.

The acidic properties of the investigated catalysts were assessed by temperature-programmed desorption (TPD) of pyridine using thermogravimetric analysis (TGA). The obtained profiles (Fig. 7) illustrate similar patterns of pyridine desorption among the analyzed samples, characterized by three distinct desorption peaks occurring around 300 °C, 390 °C, and between 600 and 640 °C. The predominant peak observed in the temperature range of 600–640 °C indicates that most of the surface acidic sites in these gabbroic rocks are strongly acidic. Notably, sample ML 32 uniquely exhibited an additional intense peak at approximately 390 °C, signifying a balanced distribution of both strong and weak acidic sites. Strong acidic sites are particularly beneficial for photocatalytic processes as they enhance surface reactivity and improve the adsorption capacity for the molecules (Jia, 2022). The relationship between specific surface area and acidic properties (Table 3) suggests that samples with higher surface areas generally exhibit a higher total quantity of acidic sites. From a photocatalytic perspective, the presence of a significant number of strong acidic sites, as seen in ML 105 and ML 05, likely facilitates improved adsorption and activation of reactant molecules, thus enhancing their potential efficacy in photocatalytic degradation reactions. Conversely, the balanced acidic profile of ML 32 may promote effective intermediate adsorption-desorption dynamics, potentially reducing recombination losses and favoring enhanced photocatalytic performance in pollutant degradation processes.

## 3.2. Catalytic tests

### 3.2.1. Photooxidation of 2-propanol and CO

The concentration-time profiles for 2-propanol oxidation (Fig. 8) reveal three distinct behaviours that depend on the balance between surface adsorption and photo-reactivity. ML 105 and ML 05 exhibit the largest initial uptake of 2-propanol in the dark, reflecting the highest specific surface areas of series (4.96 and 3.65 $m^2 g^{-1}$, respectively) and the greatest total concentration of Brønsted-type acid sites (13.5 and 11.0 μmol $g^{-1}$) that anchor the alcohol through hydrogen bonding to surface O–H groups. Upon illumination, both samples release part of the pre-adsorbed alcohol (photodesorption), after which a steady decrease resumes as the photochemical route predominates. By contrast, ML 2010 and ML 2520 show continuous removal of 2-propanol even in the dark because their lower acid–site density is compensated by mineral phases rich in Fe-bearing chlorite/serpentine that supply stronger Lewis binding centers. The photonic step simply accelerates a process that is already adsorption-limited. The net outcome is that ML 2010, which combines a moderate surface area (2.08 $m^2 g^{-1}$) with an optimal distribution of medium/strong sites, achieves the highest acetone yield (8.5 μmol/L after 21 h) and the largest rise in $CO_2$, confirming deeper mineralization. In contrast, the short average charge-carrier lifetime measured for ML 05 (0.70 ns at 325 nm excitation) limits interfacial redox turnover despite its large surface reservoir. These trends demonstrate that visible-light performance scales with the product of charge-carrier lifetime, accessible acid sites and mineralogical redox centers rather than with surface area alone.

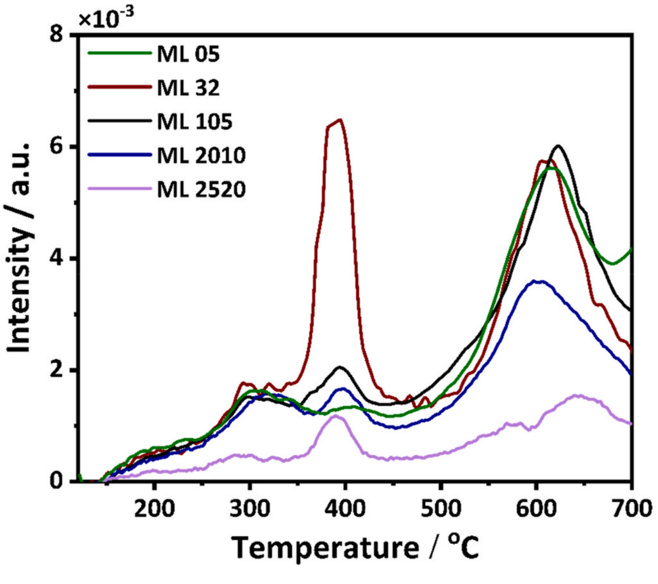

**Fig. 7.** TPD of pyridine from the surface of the studied materials.

Photo-excitation of the silicate framework (Eg = 2.0–3.1 eV) creates conduction-band electrons localised on $Fe^{2+}/Ti^{3+}$ centers and valence-band holes delocalised on lattice O 2p orbitals. The holes abstract an α-H from adsorbed 2-propanol to form the $(CH_3)_2\dot{C}OH$ radical, which rapidly dehydrogenates on adjacent Lewis acidic $Mg^{2+}/Ca^{2+}$ sites to acetone. Electrons reduce molecular $O_2$ chemisorbed on $Fe^{3+}$ sites to $O_2{\bullet}^-$; protonation yields $HO_2{\bullet}/H_2O_2$ and finally •OH, which oxidise acetone step-wise to acetate, formate and ultimately $CO_2$. Strong Brønsted sites stabilize the initial alcohol while medium-strength sites promote desorption of acetone, preventing catalyst poisoning. Simple schematic steps include: (i) band-gap excitation, (ii) hole-driven H-abstraction, (iii) electron-driven formation of superoxide/hydroxyl radicals, and (iv) sequential oxidation of acetone to $CO_2$.

CO photooxidation to $CO_2$ (Fig. 9) uncovers a different hierarchy. ML 105 and ML 32 exhibit the fastest disappearance of CO and the largest formation of $CO_2$, whereas ML 2520 has a minor photocatalytic activity. Here, intrinsic acidity is less important than the lifetime of photo-generated charges and the ability of Fe-, Mn- and Ti-bearing amphiboles to cycle between adjacent redox states. ML 32, although moderate in surface area, possesses the longest carrier lifetime (1.65 ns at 325 nm) and contains 20 wt % diopside and 17 wt % hornblende, minerals that host $Fe^{3+}/Fe^{2+}$ couples able to mediate fast electron transfer. ML 2520, dominated by plagioclase (78 wt %) and exhibiting the lowest surface area (0.56 $m^2 g^{-1}$) and acid-site concentration (2.4 μmol $g^{-1}$), lacks sufficient redox centers or adsorption capacity, explaining the absence of measurable activity.

Photocatalytic CO oxidation proceeds through initial CO chemisorption on unsaturated $Fe^{3+}$ or $Mg^{2+}$ centers to form surface carbonyl species. Valence-band holes oxidise the adsorbed CO to a $CO_2^-$ intermediate that is rapidly attacked by superoxide or surface –OH groups generated by conduction-band electrons reacting with $O_2$ and $H_2O$. The resulting $CO_2$ may either be released or react further with basic oxo-bridges to yield surface carbonates. A tentative schematic of the whole reaction therefore includes (i) CO binding to $Fe^{3+}$, (ii) hole-mediated one-electron oxidation to $CO_2^-$, (iii) electron-mediated $O_2$ activation, (iv) coupling to yield $CO_2$ and (v) subsequent carbonate trapping. Based on the results shown in Fig. 9, most of the gabbro samples are able to adsorb CO in the dark and, given the limited $CO_2$ released into the gas phase during the tests, the formation of carbonates on the surface of gabbro samples is likely. The relatively modest amount of $CO_2$ detected in the gas phase, together with literature reports on carbonate formation on oxide surfaces, suggests that a fraction of the photogenerated $CO_2$ may be transiently retained as surface carbonate/bicarbonate species; however, dedicated in-situ spectroscopic or isotopic studies would be required to confirm and quantify this effect.

These two case studies underscore that the gabbro catalysts function as natural, multi-mineral heterojunctions in which light harvesting, charge separation, adsorption and acid-base chemistry are spatially distributed over complementary mineral phases. Engineering the relative abundance of amphibole/chlorite (for redox activity) and feldspar/pyroxene (for acid sites and adsorption) therefore provides a rational route to optimize selectivity and durability in either dehydrogenation-type VOC oxidation or direct CO photo-oxidation.

### 3.2.2. Liquid-phase 4-nitrophenol photodegradation

The time-profiles of 4-nitrophenol photodegradation in Fig. 10 reveal that illumination, rather than mere adsorption, governs the

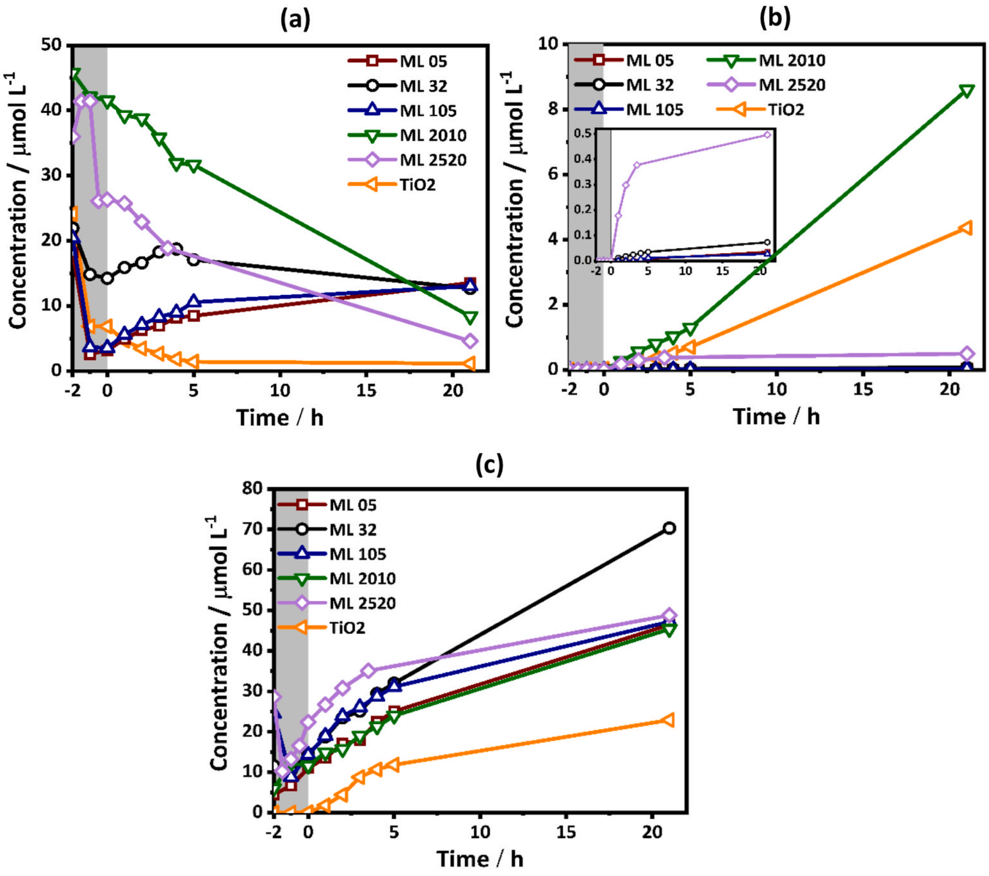

**Fig. 8.** Concentration-time profiles of a) 2-propanol, b) acetone, and c) $CO_2$ obtained during the photoreactivity tests on the analyzed gabbro samples under simulated solar radiation. The grey area shows the time without illumination.

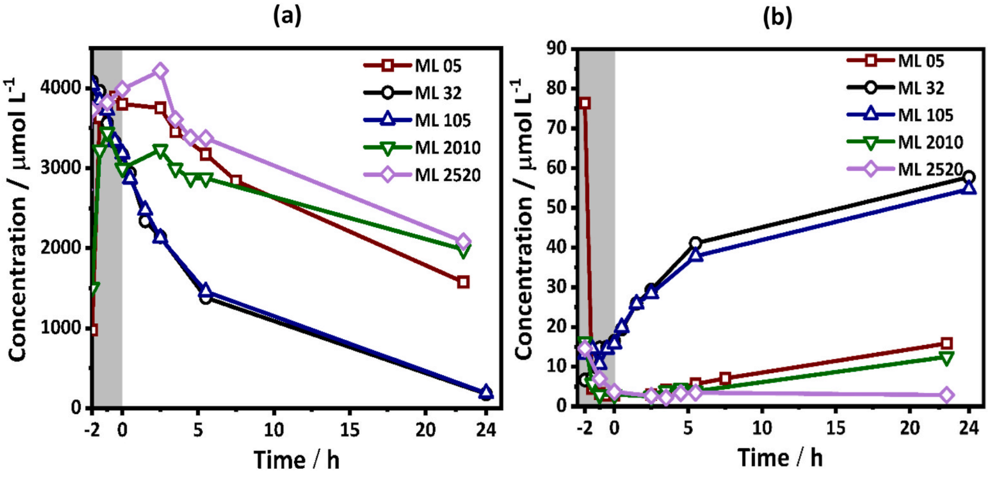

**Fig. 9.** Concentration-time profiles of a) CO and b) $CO_2$ obtained during the CO to $CO_2$ conversion tests on the analyzed gabbro samples under simulated solar radiation. The grey area shows the time without illumination.

degradation of 4-nitrophenol on the five gabbroic powders. In darkness all samples removed ≤3 % of the pollutant, whereas simulated sunlight resulted in a monotonic decrease of $c/c_0$ that, after 24 h, reached 0.35 for ML 105, 0.41 for ML 2010, 0.43 for ML 2520, 0.50 for ML 12 and 0.77 for ML 05, while anatase $TiO_2$ levelled off at 0.86. The trend mirrors the total-organic-carbon abatement measured at the end of the run i.e. 60 % for ML 105, 54 % for ML 2010, 51 % for ML 2520, 47 % for ML 12 and only 20 % for ML 05. The TOC results indicates that the disappearance of 4-nitrophenol is mainly due to its complete degradation into inorganic end-products such as $CO_2$ and water, rather than partial degradation into intermediate compounds retaining the chromophoric structure.

Three physicochemical descriptors appear to steer the activity, namely surface acidity, optical absorption energy and charge-carrier dynamics. Temperature-programmed desorption of pyridine shows that ML 105 hosts the largest population of Brønsted/Lewis sites (11 µmol $g^{-1}$) and ML 2520 the highest density per unit area (4.3 µmol $m^{-2}$), whereas ML 05 possesses many sites but of weaker strength, as evident

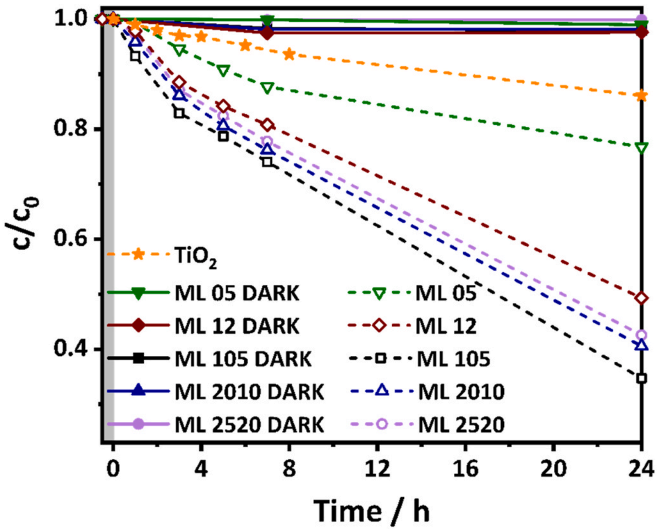

**Fig. 10.** Photooxidation of 4-nitrophenol dissolved in water in the presence of the analyzed gabbro samples under simulated sunlight (open symbols) and in the dark (full symbols).

by its dominant desorption peak below 400 °C. Strong acid sites stabilize the phenolate form of 4-nitrophenol once it is photoadsorbed on the catalyst surface from solution, orienting the nitro group toward surface holes and favoring oxidative denitration. The optical band gaps follow the order: ML 32 (2.00 eV) < ML 2010 (2.66 eV) ≈ ML 105 ≈ ML 2520 (2.77 eV) < ML 05 (3.06 eV) < $TiO_2$ (3.30 eV). Under the AM1.5 spectrum this translates into progressively smaller photon flux available for ML 05 and for anatase, which explains their inferior rate constants despite their higher BET area (4.96 and 81 $m^2$ $g^{-1}$, respectively). Finally, time-correlated single-photon-counting indicates that the longest average lifetime of 325 nm-generated excitons belongs to ML 32 (1.65 ns) and ML 105 (1.47 ns), whereas ML 05 recombines within 0.70 ns. A longer residence time of separated charges increases the probability that valence-band holes oxidise adsorbed organics before geminate recombination occurs, rationalizing the superior quantum efficiency of ML 105 and the average performance of ML 32 despite its moderate acidity.

Mineralogical and elemental evidence supports these structure-activity correlations. Hornblende and diopside, both rich in $Fe^{3+}$/$Fe^{2+}$, represent 31 wt % of ML 105, while chlorite–serpentine account for 42 wt % of ML 2010. The coupled presence of Fe/Mg silicates and trace Ti (0.08 at % in ML 105) favors intervalence charge-transfer transitions that red-shift the absorption edge and create internal $Fe^{2+}$ ↔ $Fe^{3+}$ traps able to postpone $e^-/h^+$ recombination. SEM-EDX further shows that ML 105 is enriched in Ca (8.6 at %) and Mg (6.5 at %), cations that promote Lewis acidity by polarizing surface silanols. Conversely the overwhelming plagioclase content of ML 2520 (78 wt %), although virtually non-porous (0.56 $m^2$ $g^{-1}$), still enables suitable activity thanks to its exceptionally concentrated acidic sites, evidencing that reactivity here is controlled by site quality rather than by geometrical area alone.

Taken together, these observations converge toward a classical heterogeneous photocatalytic mechanism, modulated by the mixed-oxide nature of gabbro. Upon photon absorption electrons are excited to a conduction manifold dominated by Fe 3d/Ti 3d levels, leaving holes in O 2p-based valence states. Conduction-band electrons reduce dissolved oxygen to superoxide, whereas valence-band holes and surface •OH formed from water oxidation initiate electrophilic attack on the para-nitrophenolate. Successive reactions cleave the nitro group to nitrite/nitrate, add hydroxyls to the ring, and finally open the aromatic cycle to yield short-chain acids that photomineralise to $CO_2$, as corroborated by the TOC data. Surface Brønsted sites facilitate the first deprotonation and anchor intermediates, while strong Lewis sites stabilize transient radicals long enough for oxidative fragmentation.

The schematic highlights the converging oxidative and reductive half-cycles operating on the heterogeneous surface. The coexistence of $Fe^{2+}$ and $Fe^{3+}$ centers in hornblende and chlorite not only narrows the apparent band gap but also provides internal redox couples that shuttle electrons toward adsorbed oxygen, sustaining the formation of reactive oxygen species even when UV flux is limited. This synergy between broad-band light harvesting, resilient acid sites and delayed recombination underpins the superior photomineralisation capacity of ML 105 and ML 2010 over conventional $TiO_2$, pointing to gabbro waste as a low-cost, solar-responsive catalyst for water purification.

### 3.2.3. $NO_2$ Photoreduction

The temperature-dependent experiments, in dark conditions, confirm that all five gabbro samples begin to reduce $NO_2$ only after they have been heated above about 125 °C, but the extent of conversion and the temperature at which the reaction initiates vary markedly (Fig. 11a). Sample ML 2010 is the most active, removing 17.5 % of the inlet $NO_2$ and doing so at the lowest onset temperature, while ML 2520, ML 32 and ML 105 cluster around 11–12.5 % and ML 05 reaches 13.8 %. The superior behavior of ML 2010 matches its relatively open pore system (7.1 nm average diameter) and its balanced concentration of strong acid sites

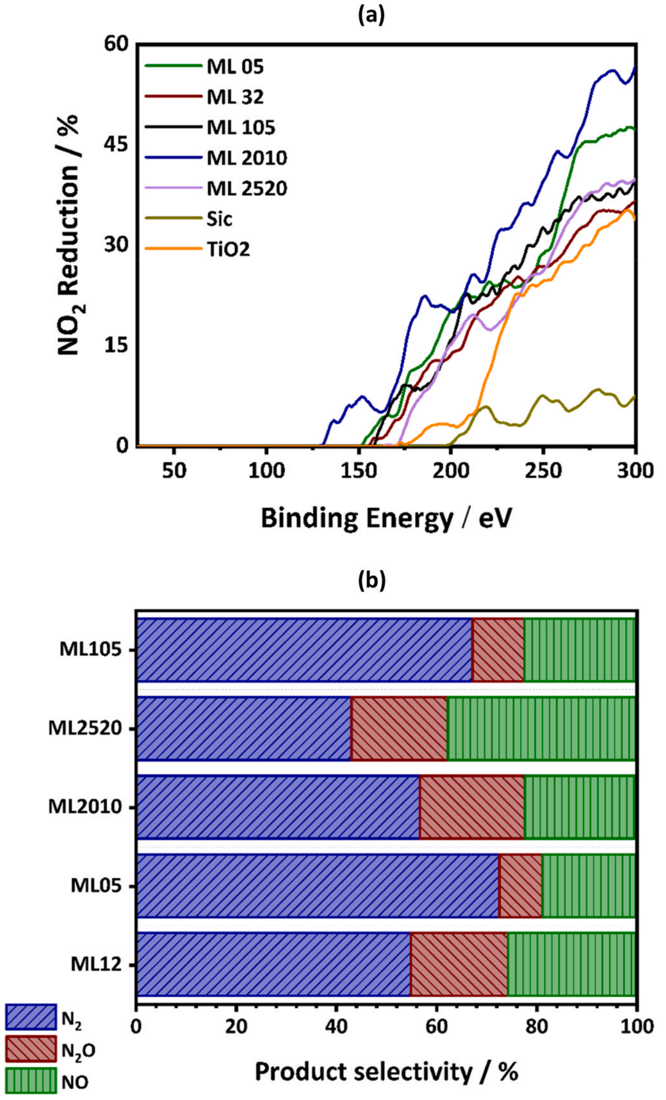

**Fig. 11.** a) Temperature-dependent relative $NO_2$ conversion on investigated gabbro samples. b) Calculated relative percentage selectivity of the three main products (NO, $N_2O$, and $N_2$) in the temperature range of 30–300 °C for the analyzed materials.

(6.9 µmol g$^{-1}$, 3.3 µmol m$^{-2}$), which favor $NO_2$ adsorption and nitrate formation without creating an over-saturated surface. X-ray diffraction shows that ML 2010 contains a high fraction of chlorite-serpentine and hornblende, phases rich in Fe and Mg that are able to shuttle electrons between Fe$^{2+}$/Fe$^{3+}$ couples during reduction steps.

Selectivity measurements give additional insight (Fig. 11b). Nitrogen is the desired product, whereas NO and $N_2O$ are undesirable intermediates due to their environmental adverse effects (Obalová, 2021). ML 05, the sample with the highest total acidity (13.5 µmol g$^{-1}$) but also the broadest distribution of acid strengths, steers the reaction most cleanly towards $N_2$, reaching about 70 % selectivity. ML 2520, with fewer but very dense Lewis sites (4.3 µmol m$^{-2}$), over-stabilizes NO* and shows only 40 % $N_2$. The comparison indicates that a mixture of moderate and strong acid sites, rather than a preponderance of either extreme, allows adsorbed $NO_x$ species to couple and desorb as $N_2$ instead of leaving the surface prematurely as NO or decomposing to $N_2O$.

When the same solids are exposed to visible light in the 30–120 °C range, the results change significantly (Fig. 12). No sample shows activity in the dark at 30 °C, but a 15-min irradiation step immediately triggers measurable conversion on every sample. Again ML 2010 responds most strongly with light-assisted conversion of 6 % at 90 °C, whereas the other samples remain near 2–3 % except ML 05, which benefits synergistically from mild heating and reaches 10 % at 90 °C. The benign response to light correlates with the measured band gaps. ML 32 has the narrowest optical gap (2.0 eV) and absorbs visible photons most efficiently, but its moderate acidity limits the surface coverage of $NO_2$ intermediates. ML 2010 and ML 105 possess slightly wider gaps (2.66–2.77 eV) yet compensate with abundant adsorption sites, so their overall photo-thermal rates are highest. The low-area ML 2520 (0.56 m$^2$ g$^{-1}$) absorbs enough light to form charge carriers but lacks adsorption capacity and therefore lags.

Taken together, the data suggest a reaction scheme in which $NO_2$ first chemisorbs as nitrate or nitrite on Lewis-acidic cation sites (mainly Mg$^{2+}$, Fe$^{3+}$ and Ca$^{2+}$ exposed at feldspar or hornblende terminations). Visible photons promote electrons from the valence band of the silicate framework (or Fe-O clusters) into the conduction band. The accompanying holes are quenched by $H_2$, generating protons that remain at the surface. Conduction-band electrons reduce adsorbed $NO_2^-$ to NO*, then further to $N_2O$*. Protons add to these intermediates, lowering activation barriers. A second electron-proton pair cleaves $N_2O$* to $N_2$ and surface OH$^-$, and the latter is re-oxidized by holes to release ½$O_2$ and regenerate the site. In concise form:

$$2H_2O + 4h^+ \rightarrow 4H^+ + O_2 \tag{1}$$

$$NO_2(ads) + 2e^- + H^+ \rightarrow NO(ads) + OH^- \tag{2}$$

$$2NO(ads) + 2e^- + H^+ \rightarrow N_2O(ads) + OH^- \tag{3}$$

$$N_2O(ads) + 2e^- + 2H^+ \rightarrow N_2 + H_2O \tag{4}$$

$$4OH^- + 4h^+ \rightarrow O_2 + 2H_2O \tag{5}$$

This sequence is facilitated by adjacent Brønsted and Lewis centers that stabilize the anionic intermediates and by the iron-bearing minerals that act as internal redox mediators. Mild heating (up to 90 °C) accelerates surface diffusion of NO* and $N_2O$*, allowing the bimolecular N–N coupling and the final $N_2O$ dissociation step to keep pace with photogenerated electrons.

The combination of low band-gap energy, a network of well-distributed acid sites and iron-rich silicate domains explains why quarry waste gabbro, despite its modest surface area, rivals or exceeds $TiO_2$ under visible light for $NO_2$ removal. By choosing rocks such as ML 2010 for rate and ML 05 for selectivity, or by blending them, one can design passive surfaces and filters that convert traffic exhaust into benign nitrogen at temperatures easily reached in hot climates or under mild solar heating.

Photothermal experiments (Fig. 13) further clarify the effect of illumination on product distribution during NO2 reduction. For both representative samples, ML 05 and ML 2010, visible-light irradiation results in high selectivity for $N_2$ even at low temperatures (30–90 °C), while the formation of NO and $N_2O$ remains limited throughout this range. Under purely thermocatalytic conditions, significant N2 formation occurs only as the reaction approaches the thermal ignition temperature (approximately 120 °C). As the temperature increases, the photothermal selectivity profiles gradually converge with those obtained in the dark, and at the ignition temperature both conditions yield comparable product distributions dominated by $N_2$. These results indicate that illumination effectively lowers the activation temperature required for $NO_2$ reduction without altering the overall reaction pathway, while simultaneously enhancing $N_2$ selectivity and suppressing the formation of undesirable intermediates at mild temperatures.

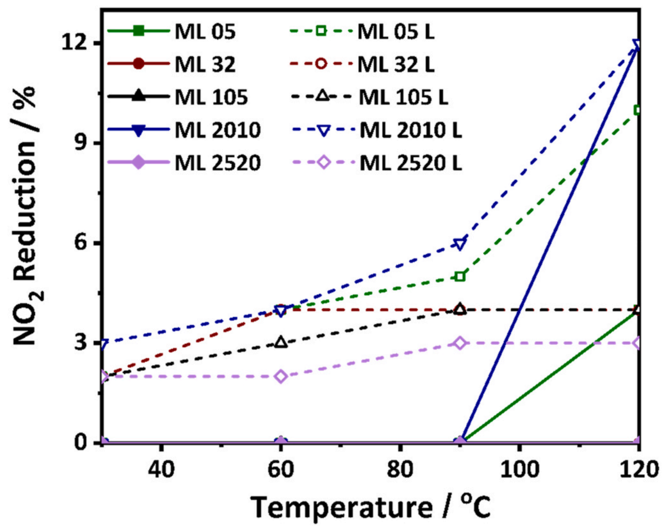

**Fig. 12.** Curves of $NO_2$ reduction in the dark as a function of temperature (solid curves with full symbols) and $NO_2$ reduction using visible light as a function of temperature (dashed curves with empty symbols) on investigated gabbro samples.

## 4. Conclusions

In this study, mafic plutonic rock samples (gabbro, olivine gabbro) collected in the United Arab Emirates were characterized and tested for the first time as photocatalysts in the oxidation of CO and 2-propanol in air under simulated solar and in the reduction of $NO_2$ under visible light irradiation. The investigated gabbro rock samples were also tested as photocatalysts in water treatment for the photodegradation of 4-nitrophenol. The $N_2$ adsorption/desorption analysis shows that the used gabbroic materials exhibit mesoporous and macroporous properties, with low specific surface areas (between 0.56 and 4.96 m$^2$/g) compared to commercial $TiO_2$. The results of the SEM-EDX analysis show that the surfaces of the analyzed rocks consist mainly of O, Si, Al, Ca, Mg and Fe, whereby the element concentrations vary considerably between the samples. The UV–vis DR analyses show that the studied gabbroic rocks have a lower band gap energy than $TiO_2$, which allows the absorption of light in both the UV and visible spectrum.

In the photodegradation runs of 2-propanol performed under simulated sunlight, ML 2010 showed the highest catalytic activity and produced 8.5 µmol/L acetone after 21 h of illumination. In the oxidation of 4-nitrophenol, ML 105 showed the highest oxidation rate (65.4 %), followed by samples ML 2010 (59.3 %) and ML 2520 (57.3 %). The samples ML 105 and ML 32 showed the highest conversion of CO to $CO_2$, and also the greater extent of adsorption of CO in the dark. Thermal catalytic $NO_2$ reduction experiments showed that all gabbro samples

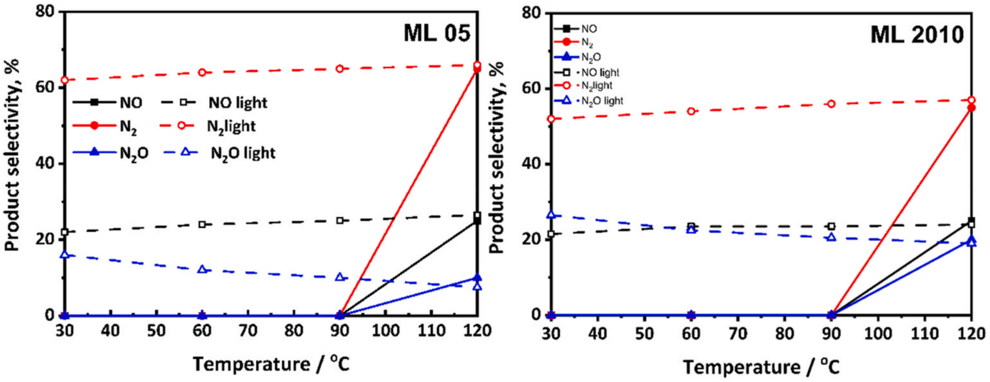

**Fig. 13.** Photothermal $NO_2$ reduction over ML 05 and ML 2010 and the related product selectivity.

effectively reduced $NO_2$ at temperatures above 125 °C, with sample ML 2010 achieving the highest $NO_2$ reduction extent of 17.5 %. The selectivity in the formation of $N_2$, the most desired product of $NO_2$ reduction, was highest for ML 05 (∼70 %) and lowest for ML 2520 (∼40 %). Photothermal $NO_2$ reduction experiments conducted between 30 and 120 °C showed that visible light illumination increased the $NO_2$ reduction rates of all gabbroic rocks analyzed. In particular, ML 2010 showed the highest photothermal catalytic activity under the studied experimental conditions. A balanced ratio of strong and moderate acidic sites improves the catalytic efficiency of the investigated gabbroic rocks by enhancing adsorption (CO to $CO_2$ photoconversion, 2-propanol conversion), surface reaction rates ($NO_2$ reduction) and desorption steps (4-nitrophenol oxidation), thus increasing the overall catalytic activity. All investigated gabbro samples showed higher photocatalytic activity than $TiO_2$ under the investigated reaction conditions.

The results of the study presented here show that the investigated gabbroic rocks have a promising potential as photocatalysts, especially for applications related to the degradation of organic and inorganic pollutants in air and water and for $NO_2$ reduction. Their broad light absorption, highly acidic sites and diverse mineral composition contribute to their functional versatility and make them a valuable alternative to conventional materials such as $TiO_2$. For the first time, this naturally occurring gabbro materials are shown to exhibit both oxidative and reductive photocatalytic properties when activated under solar radiation and can also store oxidized carbon in the form of carbonates.

## CRediT authorship contribution statement

**Gregor Žerjav:** Writing – original draft, Validation, Investigation. **Muhammad Ashraf Sabri:** Writing – review & editing, Investigation, Formal analysis. **Samar Al Jitan:** Writing – review & editing, Methodology. **Riccardo Tribuzio:** Resources, Investigation. **Hebah Jarusheh:** Writing – review & editing, Methodology, Data curation. **Albin Pintar:** Writing – review & editing, Resources. **Khalid Al-Ali:** Writing – review & editing, Supervision, Data curation. **Andrea Ceriani:** Writing – review & editing, Formal analysis. **Alessandro Decarlis:** Writing – review & editing, Supervision, Conceptualization. **Giovanni Palmisano:** Writing – review & editing, Supervision, Project administration, Conceptualization.

## Declaration of competing interest

The authors declare that they have no known competing financial interests or personal relationships that could have appeared to influence the work reported in this paper.

## Acknowledgments

Ms. Reem Al Sakkaf and Mr. Zhe Wang are acknowledged for their lab support. The Research and Innovation Center on $CO_2$ and Hydrogen at Khalifa University (project RC2-2019-007) is acknowledged for financial support and lab facilities. G. Žerjav and A. Pintar gratefully acknowledge the financial support of the Slovenian Research and Innovation Agency (research core fundings no. P2-0150 and P1-0418).

## Appendix A. Supplementary data

Supplementary data to this article can be found online at https://doi.org/10.1016/j.jenvman.2025.128278.

## Data availability

Data will be made available on request.

## References

Abdel-Hameed, S.A.M., Hamdy, Y.M., Sadek, H.E.H., 2019. Characterization and luminescence properties of Mn-Doped zinc borosilicate glasses and glass-ceramics. Silicon 11 (3), 1185–1192. https://doi.org/10.1007/s12633-017-9685-z.

Almeida, L.N.B., et al., 2022. The adsorptive and photocatalytic performance of granite and basalt waste in the discoloration of basic dye. Catalysts 12 (10), 1076. https://doi.org/10.3390/catal12101076.

Armaković, S.J., Armaković, S., 2025. Zeolite-supported TiO2 for enhanced photocatalytic performance in environmental applications: a review. Catalysts 15 (2), 174. https://doi.org/10.3390/catal15020174.

Artem'ev, A.V., et al., 2019. Luminescence of the Mn2+ ion in non-Oh and Td coordination environments: the missing case of square pyramid. Dalton Trans. 48 (43), 16448–16456. https://doi.org/10.1039/C9DT03283E, 10.1039/C9DT03283E.

Badamasi, H., et al., 2025. A review of recent advances in green and sustainable technologies for removing 4-nitrophenol from the water and wastewater. Sustain. Chem. Pharm. 43, 101867. https://doi.org/10.1016/j.scp.2024.101867.

Bertier, P., et al., 2016. On the use and abuse of N 2Physisorption for the characterization of the pore structure of shales. Filling the Gaps – from Microscopic Pore Structures to Transport Properties in Shales: Clay Minerals Society 21, 1. https://doi.org/10.1346/CMS-WLS-21-12 [Online]. Available:

Chatla, A., Almanassra, I.W., Kochkodan, V., Laoui, T., Alawadhi, H., Atieh, M.A., 2022. Efficient removal of eriochrome black T (EBT) dye and chromium (Cr) by hydrotalcite-derived mg-ca-al mixed metal oxide composite. Catalysts 12 (10). https://doi.org/10.3390/catal12101247.

Chen, K., Dong, W., Huang, Y., Wang, F., Zhou, J.L., Li, W., 2025. Photocatalysis for sustainable energy and environmental protection in construction: a review on surface engineering and emerging synthesis. J. Environ. Chem. Eng. 13 (5), 117529. https://doi.org/10.1016/j.jece.2025.117529.

Czaja, M., Lisiecki, R., Chrobak, A., Sitko, R., Mazurak, Z., 2018. The absorption- and luminescence spectra of Mn3+ in beryl and vesuvianite. Phys. Chem. Miner. 45 (5), 475–488. https://doi.org/10.1007/s00269-017-0934-x.

Devaraja, P.B., et al., 2015. Luminescence properties of MgO: Fe3+ nanopowders for WLEDs under NUV excitation prepared via propellant combustion route. Journal of Radiation Research and Applied Sciences 8 (3), 362–373. https://doi.org/10.1016/j.jrras.2015.02.001.

D'Amico, M., Messina, F., Cannas, M., Leone, M., Boscaino, R., 2009. Photoluminescence spectral dispersion as a probe of structural inhomogeneity in silica. J. Phys. Condens. Matter 21 (11), 115803. https://doi.org/10.1088/0953-8984/21/11/115803.

Eray, E., Boffa, V., Jørgensen, M.K., Magnacca, G., Candelario, V.M., 2020. Enhanced fabrication of silicon carbide membranes for wastewater treatment: from laboratory to industrial scale. J. Membr. Sci. 606, 118080. https://doi.org/10.1016/j.memsci.2020.118080.

Esparza, P., Borges, M.E., Díaz, L., 2011. Studies in a fixed-bed photocatalytic reactor System using natural materials for degradation of a dye contaminant in water. Water, Air, Soil Pollut. 218 (1), 549–555. https://doi.org/10.1007/s11270-010-0667-7.

Gaft, M., Reisfeld, R., Panczer, G., 2005. Modern Luminescence Spectroscopy of Minerals and Materials. Springer.

Gao, J., et al., 2025. Phonon involved photoluminescence of Mn2+ ions doped CsPbCl3 micro-size perovskite assembled crystals. Adv. Sci. 12 (11), 2413402. https://doi.org/10.1002/advs.202413402.

Goodenough, K.M., et al., 2010. Architecture of the Oman–UAE ophiolite: evidence for a multi-phase magmatic history. Arabian J. Geosci. 3 (4), 439–458. https://doi.org/10.1007/s12517-010-0177-3.

Guesmi, M., et al., 2023. Study of defects in fused silica via a Franck-Condon analysis. J. Lumin. 257, 119668. https://doi.org/10.1016/j.jlumin.2023.119668.

Ichikawa, J., Kominami, H., Hara, K., Kakihana, M., Matsushima, Y., 2022. Electronic structure calculation of Cr3+ and Fe3+ in phosphor host materials based on relaxed structures by molecular dynamics simulation. Technologies 10 (3). https://doi.org/10.3390/technologies10030056.

Ivanova, S., et al., 2016. Layered P3-NaxCo1/3Ni1/3Mn1/3O2 versus spinel Li4Ti5O12 as a positive and a negative electrode in a full sodium–lithium cell. ACS Appl. Mater. Interfaces 8 (27), 17321–17333. https://doi.org/10.1021/acsami.6b05075.

Jia, Y., et al., 2022. Revealing the correlation between surface acid sites and activity of VPO/TiO2 catalyst. Catal. Lett. 152 (7), 2215–2226. https://doi.org/10.1007/s10562-021-03794-3.

Kalapsazova, M., Stoyanova, R., Zhecheva, E., Tyuliev, G., Nihtianova, D., 2014. Sodium deficient nickel–manganese oxides as intercalation electrodes in lithium ion batteries. J. Mater. Chem. A 2 (45), 19383–19395. https://doi.org/10.1039/C4TA04094E, 10.1039/C4TA04094E.

Kamps, O.M., Van Ruitenbeek, F.J.A., Mason, P.R.D., Van der Meer, F.D., 2018. Near-Infrared spectroscopy of hydrothermal versus low-grade metamorphic chlorites. Minerals 8 (6). https://doi.org/10.3390/min8060259.

Karami, K., Bayat, P., Khosropour, H., Siadatnasab, F., Rezaei, B., Mardaniboldaji, A., 2021. Synthesis and characterization of a new Cu (BHB)2/Fe-MIL-101-NH2 composite: a novel hydrogen peroxide sensor based upon the Bimetallic complex. J. Electrochem. Soc. 168 (1), 017508. https://doi.org/10.1149/1945-7111/abdb46.

Kaur, A., Chahal, P., Hogan, T., 2016. Selective fabrication of SiC/Si diodes by excimer laser under ambient conditions. IEEE Electron Device Lett. 37 (2), 142–145. https://doi.org/10.1109/LED.2015.2508479.

Kumar, V., et al., 2020. Observation of unusual Griffith's phase behavior in quadruple perovskite oxide CaCu3Mn4O12 (CCMO) synthesized through chemical route. Arab. J. Chem. 13. https://doi.org/10.1016/j.arabjc.2020.01.003.

Kumar, M., Uniyal, A., Chauhan, A.P.S., Singh, S.P., 2003. Optical absorption and fluorescent behaviour of titanium ions in silicate glasses. Bull. Mater. Sci. 26 (3), 335–341. https://doi.org/10.1007/BF02707456.

Lee, H., et al., 2016. Electric field-aided selective activation for indium-gallium-zinc-oxide thin film transistors. Sci. Rep. 6 (1), 35044. https://doi.org/10.1038/srep35044.

Lee, D.-E., Kim, M.-K., Danish, M., Jo, W.-K., 2023. State-of-the-art review on photocatalysis for efficient wastewater treatment: attractive approach in photocatalyst design and parameters affecting the photocatalytic degradation. Catal. Commun. 183, 106764. https://doi.org/10.1016/j.catcom.2023.106764.

Li, M., Wang, R., 2024. Combined catalytic conversion of NOx and VOCs: present status and prospects. Materials 18 (1). https://doi.org/10.3390/ma18010039 (in eng).

Lin, J.-F., Speziale, S., Mao, Z., Marquardt, H., 2013. Effects of the electronic spin transitions of iron in lower mantle minerals: implications for deep mantle geophysics and geochemistry. Rev. Geophys. 51 (2), 244–275. https://doi.org/10.1002/rog.20010.

Liu, Z., et al., 2025. Empowering wastewater treatment with step scheme heterojunction ternary nanocomposites for photocatalytic degradation of nitrophenol. Sci. Rep. 15 (1), 3299. https://doi.org/10.1038/s41598-025-86975-z.

X. I. Llc, "XPS spectra - Aluminum compounds," ed: XPS Research Institute US.

Malik, M., Dagar, S., Hooda, A., Agarwal, A., Khasa, S., 2020. Effect of magnetic ion, Fe3+ on the structural and dielectric properties of oxychloro bismuth borate glasses. Solid State Sci. 110, 106491. https://doi.org/10.1016/j.solidstatesciences.2020.106491.

May, A.M., Dempsey, J.L., 2024. A new era of LMCT: leveraging ligand-to-metal charge transfer excited states for photochemical reactions. Chem. Sci. 15 (18), 6661–6678. https://doi.org/10.1039/D3SC05268K, 10.1039/D3SC05268K.

Obalová, L., 2021. Catalytic decomposition of N2O and NO. Catalysts 11 (6). https://doi.org/10.3390/catal11060667.

Page, P.S., Dhabekar, B.S., Bhatt, B.C., Dhoble, A.R., Godbole, S.V., 2010. Role of Ti4+ in the luminescence process of Al2O3:Si,Ti. J. Lumin. 130 (5), 882–887. https://doi.org/10.1016/j.jlumin.2009.12.029.

Pavel, M., Anastasescu, C., State, R.-N., Vasile, A., Papa, F., Balint, I., 2023. Photocatalytic degradation of organic and inorganic pollutants to harmless end products: assessment of practical application potential for water and air cleaning. Catalysts 13 (2). https://doi.org/10.3390/catal13020380.

Pennington, A.M., et al., 2020. Photocatalytic CO oxidation over nanoparticulate Au-Modified TiO2 aerogels: the importance of size and intimacy. ACS Catal. 10 (24), 14834–14846. https://doi.org/10.1021/acscatal.0c03640.

Rabouw, F.T., Prins, P.T., Villanueva-Delgado, P., Castelijns, M., Geitenbeek, R.G., Meijerink, A., 2018. Quenching pathways in NaYF4:Er3+,Yb3+ upconversion nanocrystals. ACS Nano 12 (5), 4812–4823. https://doi.org/10.1021/acsnano.8b01545.

Saito, R.E., et al., 2025. Influence of the pressure-assisted heat treatment on the photoluminescent behavior of Fe2O3, Cr2O3, and MoO3. J. Alloys Compd. 1036, 181851. https://doi.org/10.1016/j.jallcom.2025.181851.

Searle, M.P., Waters, D.J., Garber, J.M., Rioux, M., Cherry, A.G., Ambrose, T.K., 2015. Structure and metamorphism beneath the obducting Oman ophiolite: evidence from the bani hamid granulites, northern Oman mountains. Geosphere 11 (6), 1812–1836. https://doi.org/10.1130/GES01199.1.

Sherman, D.M., 1985. The electronic structures of Fe3+ coordination sites in iron oxides: applications to spectra, bonding, and magnetism. Phys. Chem. Miner. 12 (3), 161–175. https://doi.org/10.1007/BF00308210.

Singh, R.S., Singh, S.P., 2001. Spectrochemical studies on charge transfer bands due to d0, d5 and d10 ions in a sodium silicate glass. J. Mater. Sci. 36 (6), 1555–1562. https://doi.org/10.1023/A:1017569302319.

Somakumar, A.K., et al., 2023. High-Pressure near-infrared Luminescence studies of Fe3+-Activated LiGaO2. Inorg. Chem. 62 (31), 12434–12444. https://doi.org/10.1021/acs.inorgchem.3c01627.

Song, J., Jónsson, H., Corrales, L.R., 2000. Self-trapped excitons in quartz. Nucl. Instrum. Methods Phys. Res. Sect. B Beam Interact. Mater. Atoms 166–167, 451–458. https://doi.org/10.1016/S0168-583X(99)00785-5.

Sotomayor, F.J., Cychosz, K.A., Thommes, M., 2018. Characterization of micro/mesoporous materials by physisorption: concepts and case studies. Acc. Mater. Surf. Res 3 (2), 34–50.

J. Sułowska, D. Madej, B. Pokrzywka, M. Szumera, and A. Kruk, "Structural and optical properties of pure and sulfur-doped silicate–phosphate glass," Molecules, vol. 26, no. 11, doi: 10.3390/molecules26113263.

Takhar, V., Singh, S., 2025. Nanomaterials ROS: a comprehensive review for environmental applications. Environ. Sci. Nano 12 (5), 2516–2550. https://doi.org/10.1039/D5EN00049A, 10.1039/D5EN00049A.

Taran, M.N., Langer, K., Platonov, A.N., Indutny, V., 1994. Optical absorption investigation of Cr3+ ion-bearing minerals in the temperature range 77–797 K. Phys. Chem. Miner. 21 (6), 360–372. https://doi.org/10.1007/BF00203294.

Tolj, D., et al., 2021. Synthesis of murunskite single crystals: a bridge between cuprates and pnictides. Appl. Mater. Today 24, 101096. https://doi.org/10.1016/j.apmt.2021.101096.

Wang, S., Li, X., Lai, C., Zhang, Y., Lin, X., Ding, S., 2024. Recent advances in noble metal-based catalysts for CO oxidation. RSC Adv. 14 (42), 30566–30581. https://doi.org/10.1039/D4RA05102E, 10.1039/D4RA05102E.

Wang, K., Li, K., Zhao, S., Ran, Z., Wang, F., 2025. Experimental and mechanism investigation on CO catalytic oxidation performance based on CuMn2O4 catalysts. Appl. Catal. Gen. 692, 120091. https://doi.org/10.1016/j.apcata.2024.120091.

Wei, W., et al., 2019. Effect of the Fe3+ concentration on the upconversion luminescence in NaGdF4:Yb3+, Er3+ nanorods prepared by a hydrothermal method. J. Mater. Sci. 54 (20), 13200–13207. https://doi.org/10.1007/s10853-019-03818-9.

WHO Global Air Quality Guidelines. Particulate Matter (PM2.5 and PM10), Ozone, Nitrogen Dioxide, Sulfur Dioxide and Carbon Monoxide, 2021.

Wu, J., Zhong, L., 2025. Prediction of by-product generation in gaseous ultraviolet photocatalytic oxidation processes. J. Hazard Mater. 494, 138767. https://doi.org/10.1016/j.jhazmat.2025.138767.

Xue, T., et al., 2024. Photocatalytic NOx removal and recovery: progress, challenges and future perspectives. Chem. Sci. 15 (24), 9026–9046. https://doi.org/10.1039/D4SC01891E, 10.1039/D4SC01891E.

Ye, Y., Wang, L., Hu, X., Bu, Z., 2025. Studies on the coating Formation and structure property for plasma electrolytic oxidation of AZ31 Magnesium alloy. Coatings 15 (7). https://doi.org/10.3390/coatings15070846.

Yu, X., et al., 2024. Advances in photothermal catalysis for air pollutants. Chem. Eng. J. 486, 150192. https://doi.org/10.1016/j.cej.2024.150192.

Zhang, Y., et al., 2022. Photocatalytic oxidation for volatile organic compounds elimination: from fundamental research to practical applications. Environ. Sci. Technol. 56 (23), 16582–16601. https://doi.org/10.1021/acs.est.2c05444.

Zhang, G., Ge, Q., Sun, P., 2025. Efficient photocatalytic degradation of p-Nitrophenol by Ag@Co-MOF prepared based on 1,3-Phenylenediacetic acid. Appl. Organomet. Chem. 39 (7), e70245. https://doi.org/10.1002/aoc.70245.